

Rotorcraft Aerodynamics Models for a Comprehensive Analysis

Wayne Johnson
Johnson Aeronautics
Palo Alto, California

Recent developments of the aerodynamics models for the comprehensive analysis CAMRAD II are described, particularly the unsteady aerodynamic models and dynamic stall models, and the free wake geometry calculation. Three models for the unsteady aerodynamic loads in attached flow are implemented: from incompressible thin-airfoil theory, from ONERA EDLIN, and from Leishman-Beddoes. Five dynamic stall models are implemented: from Johnson, Boeing, Leishman-Beddoes, ONERA EDLIN, and ONERA BH. A key feature of the implementation of these models is revisions allowing the retention of airfoil tables for static loads in all cases. Results are presented for a two-dimensional airfoil, a three-dimensional wing, and rotors. Extensions of the CAMRAD II free wake method to include hover and ground effect are described, including hover performance correlation.

Notation

A	rotor disk area, πR^2
c_{dz}, c_{mz}	section drag and moment coefficients at zero lift
c_l, c_d, c_m	section lift, drag, and moment coefficients
c_n	section normal force coefficient
C_L	wind axis rotor lift force, $L / \rho A (\Omega R)^2$
C_P	rotor power, $P / \rho A (\Omega R)^3$
C_T	rotor thrust, $T / \rho A (\Omega R)^2$
C_X	wind axis rotor drag force, $X / \rho A (\Omega R)^2$
D	wake geometry distortion
f	trailing-edge separation point (fraction chord from leading edge)
k	reduced frequency, frequency \times semichord/speed
M	Mach number
M_{at}	advancing tip Mach number, $(1+\mu)M_{tip}$
M_{tip}	tip Mach number, $\Omega R / (\text{speed of sound})$
r	blade radial station
r_{Betz}	initial radial station of tip vortex, Betz rollup
r_{TV}	initial radial station of tip vortex
R	blade radius
t	time
v_{conv}	wake convection velocity
α	angle of attack

α_d	delayed angle of attack
α_z	zero lift angle of attack
Γ	bound circulation
μ	advance ratio, (flight speed)/ ΩR
ρ	air density
σ	rotor solidity, (blade area)/A
τ	wake age
τ_K	extent of initial convection (wake age)
Ω	rotor rotational speed

Introduction

CAMRAD II is an aeromechanical analysis of helicopters and rotorcraft that incorporates a combination of advanced technology, including multibody dynamics, nonlinear finite elements, and rotorcraft aerodynamics. For the design, testing, and evaluation of rotors and rotorcraft; at all stages, including research, conceptual design, detailed design, and development; it calculates performance, loads, vibration, response, and stability; with a consistent, balanced, yet high level of technology in a single computer program; applicable to a wide range of problems, and a wide class of rotorcraft. Such capability is essential for helicopter problems, which are inherently complex and multidisciplinary.

A comprehensive helicopter analysis must calculate performance, loads, vibration, response, and stability. The multidisciplinary nature of helicopter problems means that similar models are required for all of these jobs. It follows that a comprehensive analysis must have a rotor wake

Revised version of paper presented at the American Helicopter Society 54th Annual Forum, Washington, DC, May 20–22, 1998. Copyright © 1999 by Wayne Johnson. All rights reserved.

model; account for drag and stall of the rotor blades; include nonlinear dynamics of the rotor and airframe; and model the entire aircraft. The analysis must perform trim, transient, and flutter tasks. The trim task finds the equilibrium solution (constant or periodic) for a steady state operating condition. The operating condition can be free flight (including level flight, steady climb or descent, and steady turns), or constrained (such as a rotor in a wind tunnel, with typically the thrust and flapping trimmed to target values). It is usually necessary to identify the control positions and aircraft orientation required to achieve the specified operating condition. The transient task numerically integrates the equations in time (from the trim solution), for a prescribed excitation. The flutter task obtains and analyzes differential equations for the system, linearized about trim (probably by numerical perturbation).

A modern comprehensive analysis must be able to analyze arbitrary configurations — whatever the designers can invent. The system configuration must be defined and changed by input to the analysis; it should not be necessary to change the code as long as the required physics are available. The definition of the solution procedure must be just as flexible as the definition of the configuration. The solution procedure must be defined and changed by input to the analysis; it should not be necessary to change the code as long as the required methods are available. CAMRAD II uses a building-block approach to achieve flexibility in the model of the dynamic and aerodynamic configuration, and in the solution procedure. The mathematical model of the kinematics, dynamics, and response allows nonlinearities (structural, aerodynamic, and kinematics); and arbitrary large motion, including rigid body motions and large rotations of components relative to each other. Hence CAMRAD II can model the true geometry of a rotorcraft, including multiple load paths (such as a swashplate and control system, lag dampers, tension/torsion straps, and bearingless rotors); vibration control devices (such as pendulum absorbers or active control); arbitrary elastic axis and arbitrary hinge order; drooped and swept tips; and dissimilar blades. The building-block approach, separating the specification of the configuration, the aeromechanical model, and the solution procedure, is essential for expandability of the analysis. Otherwise the smallest change involves the entire analysis, and growth becomes increasingly harder as each new feature is added. The building-block approach also leads naturally to more general and more rigorous models. For ease of use, a shell is provided to build typical rotorcraft and rotor models, while the core input capability always gives complete flexibility to define and revise the model. The system pieces (building blocks) constitute the core analysis. The rotorcraft shell constructs the core input for an aircraft with one or two or more rotors; in free flight or

in a wind tunnel; and an N-bladed rotor, with an articulated, hingeless, teetering, gimbaled, or bearingless hub; perhaps with a swashplate. The aerodynamic model includes a wake analysis to calculate the rotor nonuniform induced-velocities, using rigid, prescribed or free wake geometry. CAMRAD II is described in references 1 and 2.

Flexibility and generality of the system configuration are obtained by assembling standard components with standard interfaces, and solving the system using standard procedures. Components perform most computations associated with the physics of the model of the system. So components are the focus of modelling issues, including the empiricism and approximations needed for a practical model of many real systems. Development of an improved model requires the development of a new component, which will fit into the existing analysis framework.

This paper describes recent developments of the aerodynamics models for the comprehensive analysis CAMRAD II. The focus is on features of the wing component: unsteady aerodynamic models (thin-airfoil theory for loads at low angle of attack), and dynamic stall models; and the wake geometry components. Several models are implemented for the unsteady aerodynamic loads in attached flow: from incompressible thin-airfoil theory, from ONERA EDLIN, and from Leishman-Beddoes. Several dynamic stall models are implemented: from Johnson, Boeing, Leishman-Beddoes, ONERA EDLIN, and ONERA BH. Extensions of the CAMRAD II free wake method to include hover and ground effect are described.

Wing Component

The CAMRAD II wing component is based on lifting-line theory, using steady two-dimensional airfoil characteristics and a vortex wake. Lifting-line theory assumes that the wing has a high aspect ratio, or more generally that spanwise variations of the aerodynamic environment are small. This assumption allows the problem to be split into separate wing and wake models, which are solved individually and combined. Viscous and compressibility effects are included by using experimental data for the two-dimensional airfoil characteristics that are the foundation for the wing solution. Corrections for yawed and swept flow are introduced, and an estimate of the spanwise drag. For low angles of attack, thin-airfoil-theory results are used to calculate the unsteady loading. For high angles of attack, an empirical dynamic stall model can be used.

Unsteady Airfoil Motion

Unsteady lift and moment in attached flow are calculated based on thin-airfoil theory. Models from incompressible thin-airfoil theory, ONERA EDLIN, and Leishman-

Beddoes are implemented. The equations for these models are given in Appendix A. Often only the unsteady, noncirculatory terms are required, since steady loads are obtained from the airfoil tables and lift deficiency function effects are usually accounted for in the wake-induced velocity. The following modifications are introduced for all three models: (a) The steady loads are excluded. (b) The moment about the quarter chord (theoretical aerodynamic center) is used for the moment about the actual aerodynamic center. (c) The loads are corrected to get the real lift-curve slope. (d) The expressions are extended to reverse flow.

The incompressible unsteady loads are derived following reference 3. For an airfoil with a trailing-edge flap, the unsteady loads are derived following references 3 to 5. Optionally the flap can be aerodynamically balanced, with an open or sealed gap.

The ONERA EDLIN (Equations Differentielles Lineaires) theory for the unsteady loads is presented in reference 6. The "extended model" of Petot includes the effects of heave as well as pitch, and time-varying free stream. The "pitch model" (see also refs. 7 to 9) is not appropriate since at high frequency it either gives a lift deficiency function approaching zero instead of one-half, or it neglects a lift-from-pitch term (depending on the interpretation of the terms in the equation). In the absence of stall, Petot found that thin-airfoil-theory results compared well with measured behavior. To include the effects of compressibility, Küssner's coefficients are used, as tabulated by van der Vooren (ref. 10) and curve-fit by Petot (ref. 6). An additional modification is made here: a constant is changed so the incompressible circulatory loads match the lift deficiency function value of $C = .5$ at high frequency. Then compared with the incompressible unsteady loads result, the ONERA EDLIN model (see Appendix A) introduces factors that are functions of Mach number; and adds a first-order differential equation for a lift increment, to account for the airfoil shed wake effects (lift deficiency function). These factors give a good representation of Küssner's coefficients, except that the moment produced by heave is always real, when it should exhibit a phase shift for nonzero Mach number. For an airfoil with a trailing-edge flap, the effects of compressibility are approximated by using these same factors in the incompressible results. No shed wake terms are included in the unsteady loads for flap lift or flap moment.

The Leishman-Beddoes theory for unsteady loads in attached flow is presented in references 11 to 13. The theory is based on the indicial response of a thin airfoil in compressible flow to heave, pitch, and flap motions. The indicial response is a combination of impulsive (small time) and circulatory (long time) terms, each approximated

by exponential functions of time. In this form, the equations for the loads can be transformed from indicial response to Laplace domain, and thence to state equations (ordinary differential equations in time). The impulsive indicial response is derived using piston theory, which is valid for nonzero Mach number and small enough time. Thus while giving nonsingular results at zero Mach number, this theory does not include the incompressible limit exactly. The amplitude of the circulatory indicial response is obtained from the quasistatic incompressible response. An additional modification is made here: for an airfoil with a trailing-edge flap, the expressions are extended to include the effects of aerodynamic balance, and to include the flap hinge moment produced by pitch and heave. The resulting unsteady loads are obtained from first-order differential equations for both the impulsive and the circulatory terms (see Appendix A). This theory includes the effects of the airfoil shed wake, but not entirely in the "circulatory" terms. Care must be taken with a vortex wake or dynamic inflow model that the shed wake effects are neither omitted nor duplicated.

Dynamic Stall

Dynamic stall is characterized by a delay in the occurrence of separated flow produced by the wing motion, and high transient loads induced by a vortex shed from the leading edge when stall does occur. Dynamic stall models from Johnson, Boeing, Leishman-Beddoes, and ONERA EDLIN, and ONERA BH are included. The equations for these models are given in Appendix B. As implemented, the dynamic stall models still use the airfoil table for steady characteristics, evaluated at an angle of attack that includes the dynamic stall delay. Retaining the use of airfoil table data is considered essential, both to provide the basic characteristics associated with airfoil shape, and to isolate the effects of the dynamic stall model. In addition to the delayed angle of attack, coefficient increments are defined by the dynamic stall model. All the models are extended to reverse flow. Let α_d be the delayed angle of attack, calculated from the angle of attack α . Then the corrected coefficients are:

$$c_l = \frac{\alpha - \alpha_z}{\alpha_d - \alpha_z} c_{l\ 2D}(\alpha_d) + \Delta c_{l\ DS} + c_{l\ US}$$

$$c_d = \left(\frac{\alpha - \alpha_z}{\alpha_d - \alpha_z} \right)^2 (c_{d\ 2D}(\alpha_d) - c_{dz}) + c_{dz} + \Delta c_{d\ DS} + c_{d\ US}$$

$$c_m = \frac{\alpha - \alpha_z}{\alpha_d - \alpha_z} (c_{m\ 2D}(\alpha_d) - c_{mz}) + c_{mz} + \Delta c_{m\ DS} + c_{m\ US}$$

where α_z is the zero-lift angle of attack, and c_{dz} and c_{mz} are the corresponding drag and moment. The form of the lift and moment corrections ensures that the coefficients below stall are unchanged. The Δc_{DS} 's are increments defined by the dynamic stall model, generally attributed to

the leading-edge vortex. Note that for use in the wing component of CAMRAD II, corrections for yawed flow are required as well. The unsteady loads in attached flow are included in the above expressions (c_{lUS}). Since these loads are calculated based on linear (thin-airfoil) theory, they can be evaluated separately and added to obtain the total loads. Optionally the unsteady loads can be set to zero for stalled flow; however, most of the dynamic stall models have been developed assuming that the attached flow terms are active at high angle of attack as well.

The Johnson dynamic stall model (adapted from refs. 14 to 17) uses an angle of attack delay proportional to $\dot{\alpha}$, plus impulsive lift and moment increments from the leading-edge vortex. Thus the model has first-order differential equations for the delayed angle of attack, and algorithms to evaluate the load increments produced by the leading-edge vortex.

The Boeing dynamic stall model (developed in refs. 18 to 20) uses an angle of attack delay proportional to the square-root of $\dot{\alpha}$, which produces the basic hysteresis effects. The coefficient increments produced by the leading-edge vortex are not used in this model. The delayed angle of attack is calculated directly from the current α and $\dot{\alpha}$ values; or using a first-order differential equation.

The Leishman-Beddoes dynamic stall model (refs. 21 to 23) uses a delayed angle of attack, plus lift and moment increments from the leading-edge vortex. This model characterizes the airfoil static stall behavior by the trailing-edge separation point f (fraction of chord from leading edge), and a critical lift coefficient c_{lCR} at the separation onset boundary (leading-edge separation at low Mach number, shock reversal at high Mach number). The airfoil data for lift are used to identify constants s_1 , s_2 , and α_s that generate $f(\alpha)$ as follows:

$$f = 1 - .3 e^{(|\alpha - \alpha_z| - \alpha_s)/s_1} \quad \text{for } |\alpha - \alpha_z| \leq \alpha_s$$

$$f = .04 + .66 e^{(\alpha_s - |\alpha - \alpha_z|)/s_2} \quad \text{for } |\alpha - \alpha_z| > \alpha_s$$

Then $|\alpha - \alpha_z| = \alpha_s$ or $f = .7$ is taken as the definition of stall. The parameters c_{lCR} , s_1 , s_2 , and α_s are required as a function of Mach number, for positive and negative angle of attack, normal and reverse flow, at each span station. The Leishman-Beddoes model for unsteady flow is based on $f_d = f(\alpha_d)$ at the delayed angle of attack.

Here the Leishman-Beddoes model is modified to use the static loads directly from the airfoil tables, instead of fitting the static loads to analytical functions. Leishman and Beddoes (ref. 21) write the static normal force, moment, and drag as functions of f :

$$c_n 2D = c_n \alpha(M) K_N(f) (\alpha - \alpha_z)$$

$$c_m 2D = c_{mz} + c_n K_M(f)$$

$$c_d 2D = c_{dz} + (1 - \eta K_D(f)) (\alpha - \alpha_z)^2$$

The Kirchhoff expression $K_N = (1/4)(1 + \sqrt{f})^2$ is used; several functional forms of K_M and K_D are found in the literature. In unsteady flow, a delayed separation point f_d is calculated from f , and then the loads evaluated using f_d (Leishman and Beddoes use the notation f''' instead of f_d); and terms for attached flow and the leading edge vortex added. Since f_d corresponds to a delayed angle of attack, it is possible to replace the analytical functions K with the loads from airfoil tables:

$$\begin{aligned} c_n &= c_n \alpha(M) K_N(f_d) (\alpha - \alpha_z) + \Delta c_{nDS} + c_{nUS} \\ &= \frac{\alpha - \alpha_z}{\alpha_d - \alpha_z} c_n \alpha(M) K_N(f_d) (\alpha_d - \alpha_z) + \Delta c_{nDS} + c_{nUS} \\ &= \frac{\alpha - \alpha_z}{\alpha_d - \alpha_z} c_n 2D(\alpha_d) + \Delta c_{nDS} + c_{nUS} \end{aligned}$$

$$\begin{aligned} c_m &= c_{mz} + c_n K_M(f_d) + \Delta c_{mDS} + c_{mUS} \\ &= c_{mz} + \frac{\alpha - \alpha_z}{\alpha_d - \alpha_z} (c_m 2D(\alpha_d) - c_{mz}) + \Delta c_{mDS} + c_{mUS} \end{aligned}$$

$$\begin{aligned} c_d &= c_{dz} + (1 - \eta K_D(f_d)) (\alpha - \alpha_z)^2 + \Delta c_{dDS} + c_{dUS} \\ &= c_{dz} + \left(\frac{\alpha - \alpha_z}{\alpha_d - \alpha_z} \right)^2 (c_d 2D(\alpha_d) - c_{dz}) + \Delta c_{dDS} + c_{dUS} \end{aligned}$$

No change to the model is implied for lift and moment, since these analytical functions are intended to be equivalent to the airfoil table data. A change is implied for the drag equation only if K_D depends on other variables besides f . There will be some changes in the resulting loads however, when the K functions do not give a good representation of the airfoil table data. At this point the lift rather than the normal force can be used. While the function $f(\alpha)$ should be identified from the normal force data, there is usually little difference if it is identified from the lift data instead. Similarly, c_{nDS} can be used for c_{lDS} ; and c_{dDS} derived from c_{nDS} . Further modifications of the model are required because the above expression for $f(\alpha)$ does not distinguish between positive and negative angle of attack. In order to handle oscillations through α_z , a continuous monotonic function of α is needed. The function f is also modified in order to handle large angle of attack. This modification to the definition of f does not affect the model for attached flow or around stall, but with it the delayed angle of attack behaves reasonably at very large angles.

In the Leishman-Beddoes dynamic stall model, the delayed angle of attack α_d is calculated including: static hysteresis around stall; a lag in the leading-edge pressure relative c_l ; and an additional lag in the boundary layer

response. There are separate α_d equations for lift and moment, to allow different behavior during reattachment. Vortex lift accumulation begins at the onset of stall, driven by the difference between the linear and nonlinear lifts, c_v . The vortex loads Δc_{DS} are obtained from c_v with a time lag. Thus the model has first-order differential equations for the delayed angle of attack and the leading-edge vortex lift.

The ONERA EDLIN (Equations Differentielles Lineaires) dynamic stall model (ref. 6) uses a stall delay, plus lift, drag, and moment increments calculated from second-order differential equations. The "extended model" of Petot includes the effects of heave as well as pitch, and time-varying free stream. Generalizations based on Petot's "pitch model" (see ref. 7) lead to more complicated equations. The load is divided into two parts. The first part is the load in the absence of stall, which here gives the unsteady load for attached flow. The second part of the load is driven by the difference between the linear load extrapolated to the unstalled domain, and the real nonlinear static load. Tests show that dynamic stall occurs at a higher angle of attack than does static stall. The absence of stall is preserved in the model by forcing the difference between the linear and nonlinear loads to be zero for a time τ_d after exceeding the static stall angle. Here the model is modified in several ways. The static and unsteady terms are separated from the dynamic stall effects. A pitch rate term in the lift, that reference 6 associates with attached flow unsteady loads, is here contained in the dynamic stall load. The loads are written in terms of $\dot{\alpha}$. Reference 6 uses the upwash rate of change \dot{w} in order to include the effects of time-varying free stream, but for a three-dimensional wing $\dot{\alpha}$ also includes the wake-induced velocity. For all the dynamic stall models, the option is available to evaluate $\dot{\alpha}$ from \dot{w} .

The ONERA BH (Bifurcation de Hopf) dynamic stall model (ref. 24) uses a delayed angle of attack, plus lift and moment increments calculated from first-order and second-order differential equations. The Hopf bifurcation model replaces the time-invariant equilibrium state of flow by a time-varying equilibrium state, as the angle of attack exceeds a critical value. The load is divided into two parts, a "steady" part (static plus attached flow unsteady) and an "unsteady" part (dynamic stall). The ONERA EDLIN theory can be used for the unsteady load in attached flow. For time-varying airfoil motion, the loads are evaluated at a delayed angle of attack that is calculated as in the Leishman-Beddoes dynamic stall model. There are also dynamic stall load increments, driven by the pitch rate and pitch acceleration. Here the model is modified by separating the static and unsteady terms from the dynamic stall effects.

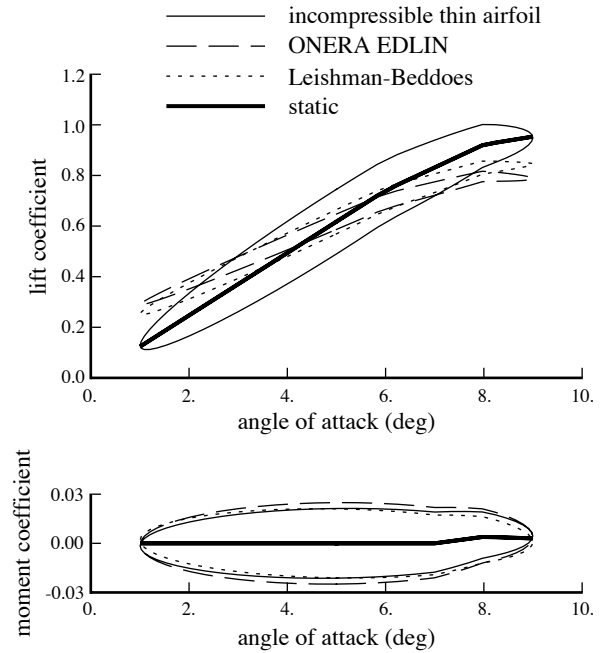


Figure 1. Two-dimensional airfoil lift and moment, at $k = .188$ and $M = .5$; oscillating in pitch, with circulatory terms.

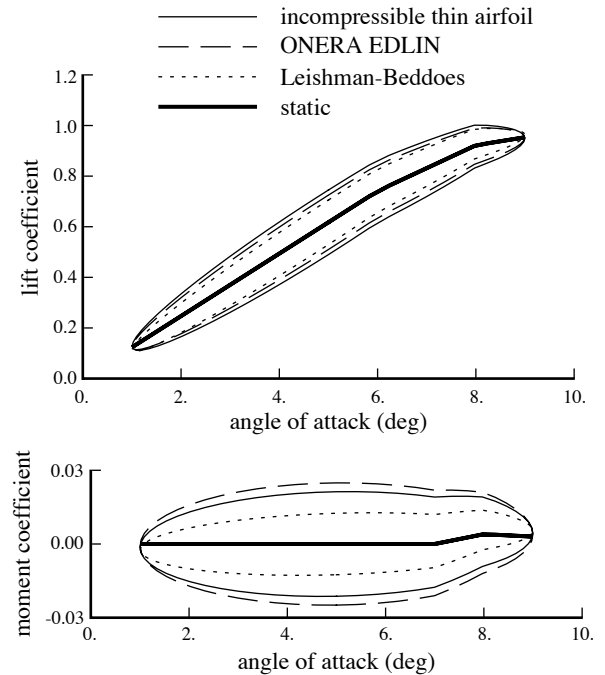


Figure 2. Two-dimensional airfoil lift and moment, at $k = .188$ and $M = .5$; oscillating in pitch, without circulatory terms.

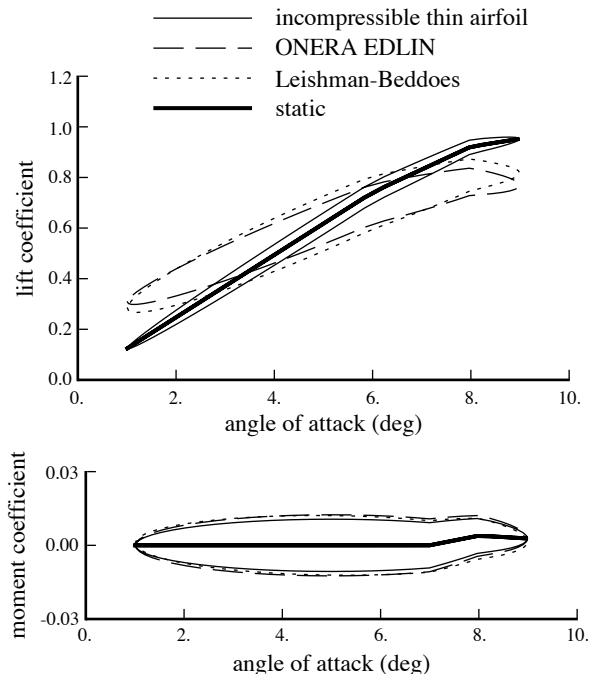


Figure 3. Two-dimensional airfoil lift and moment, at $k = .188$ and $M = .5$; oscillating in heave, with circulatory terms.

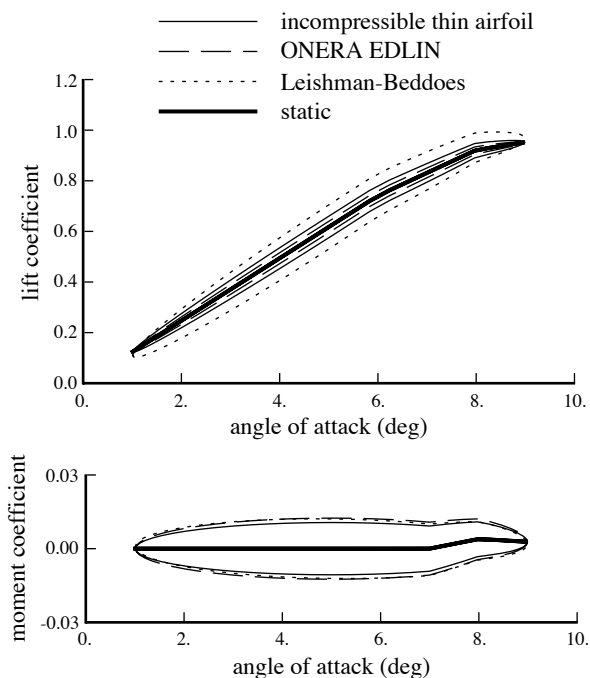


Figure 4. Two-dimensional airfoil lift and moment, at $k = .188$ and $M = .5$; oscillating in heave, without circulatory terms.

Solving the State Equations

Some of the above models introduce ordinary differential equations for aerodynamic state variables. These differential equations can be solved in CAMRAD II along with the structural dynamic equations. There are a large number of states however, and the equations can be nonlinear as well as time-varying. So an implicit solution, implemented within the wing component, is more useful for the trim and transient tasks. The equations must be formulated as differential equations in order to be linearized in the flutter task, although a linearized solution of the highly nonlinear aerodynamics involved in dynamic stall is not entirely consistent. Two implicit methods are implemented in CAMRAD II to solve the differential equations: a finite-difference solution, based on trapezoidal integration; and a sampled-data solution, based on the convolution integral or Duhamel's integral (ref. 21).

Unsteady Load Examples

Figures 1 to 4 compare the lift and moment calculated by the three unsteady aerodynamic models, for a two-dimensional NACA 0012 airfoil oscillating in pitch or heave. The ONERA EDLIN and Leishman-Beddoes models give somewhat different lift deficiency functions at this condition (figures 1 and 3; the incompressible model does not include the lift deficiency function). The "circulatory" terms of the Leishman-Beddoes model are not just shed wake effects, so omitting these terms gives different results than for the ONERA EDLIN model (figures 2 and 4).

Figures 5 and 6 compare the aerodynamic models for a three-dimensional semispan wing in a wind tunnel, oscillating in pitch about the quarter chord. The measured data are from reference 25. Two cases are considered. The case with mean angle of attack of 11 deg is used to compare the models for unsteady loads in attached flow. The case with mean angle of attack of 15 deg is used to compare the models for dynamic stall. The analysis considered a full span wing of aspect ratio 10, with 25 spanwise collocation points. The circulatory terms were included in the unsteady aerodynamic models, so the wake model included only trailed vortex elements, omitting shed vortex elements. A transient calculation was performed, using 25 to 40 time steps per cycle; the loads converged after three cycles. The wing had an NACA 0015 airfoil section. Static airfoil data were obtained from a two-dimensional test of this wing. Span stations are measured from zero at the full-span wing centerline, to one at the wing tip.

Figure 5 shows the lift and moment at 25% span station for the mean $\alpha = 11$ deg case, comparing the three unsteady aerodynamics models. Although the oscillation is at low angle of attack for this case, the dynamic stall

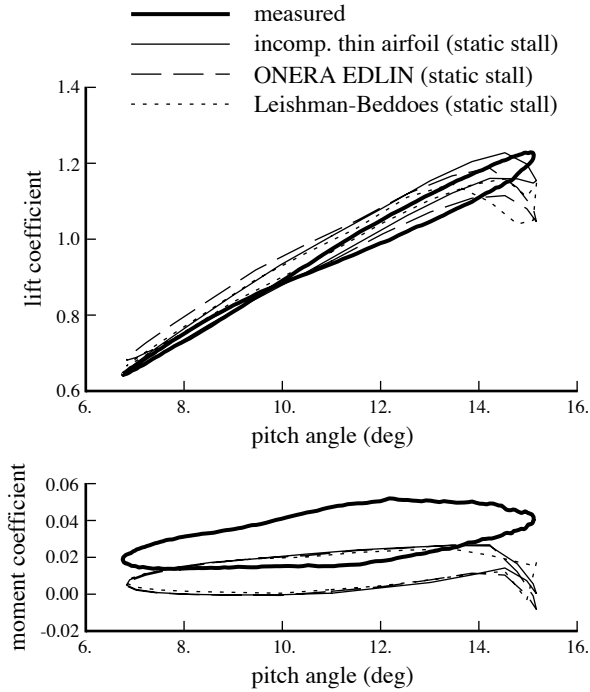


Figure 5. Three-dimensional wing oscillating in pitch, at $k = .096$ and $M = .287$; lift and moment at 25% span station (static stall).

models would improve the correlation above $\alpha = 14$ deg. The difference between measured and calculated mean moment is found along the entire span, so it should not be an effect of three-dimensional aerodynamics.

Figure 6 shows the lift and moment at 47.5% span station for the mean $\alpha = 15$ deg case, comparing the five dynamic stall models. The reduced frequency of the oscillation is typical of the once-per-revolution angle of attack variation of a helicopter blade, but the 4 deg amplitude is relatively small, resulting in a low pitch rate (maximum $\dot{\alpha}c/V = .0053$). The differences between the dynamic stall calculations are no more than should be expected from empirical models. The correlation may be judged remarkably good considering the simplicity of some of the dynamic stall models; and also exhibiting significant errors, as expected with empirical models.

A Puma helicopter with experimental swept-tip rotor blades was flight tested by the Royal Aeronautical Establishment at Bedford (ref. 26). The flight test case at high speed has a large value of cyclic pitch, hence a large contribution from the unsteady aerodynamic loads. The calculations were performed for an elastic rotor, trimming thrust and flapping with collective and cyclic pitch. The thrust, flapping, and shaft angle were obtained from the flight test data. Since the loading at high speed is negative on the advancing tip, the dual-peak wake model was used,

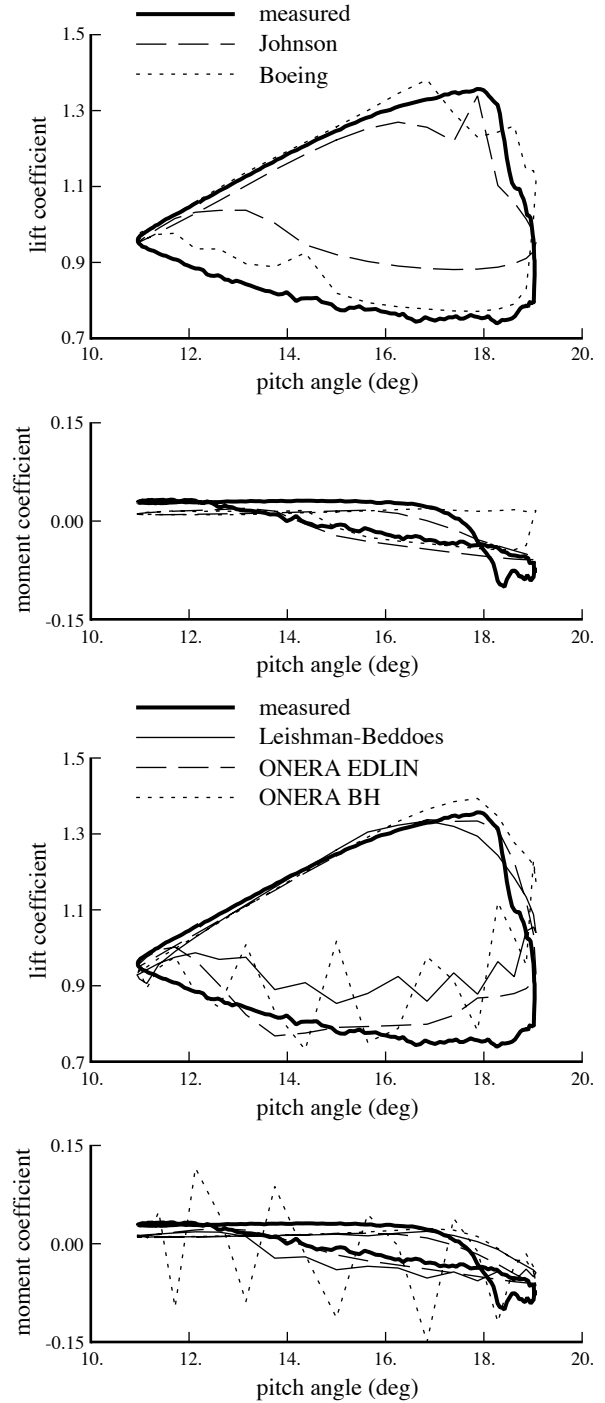


Figure 6. Three-dimensional wing oscillating in pitch, at $k = .038$ and $M = .287$; lift and moment at 47.5% span station, with dynamic stall model.

with rigid wake geometry. Figures 7 and 8 show the normal force and moment for an advance ratio of $\mu = .38$, advancing tip Mach number $M_{at} = .86$, and thrust $C_T/\sigma = .080$; at 92% radius (on the swept tip). The flight test measurements are compared with results using the three

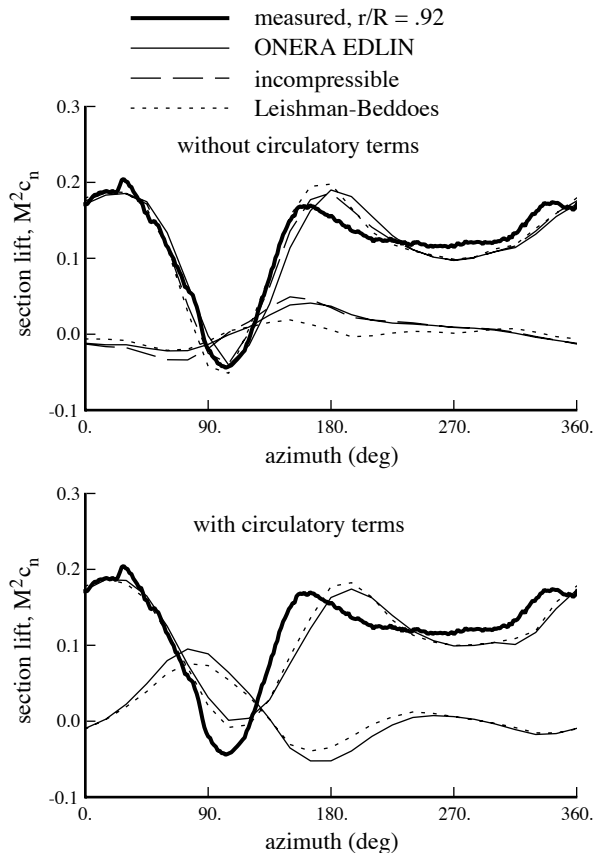


Figure 7. Flight test of Puma with swept tip rotor blade, at $\mu = .38$, $M_{at} = .86$, and $C_T/\sigma = .080$; total section lift and unsteady lift.

models for unsteady aerodynamics. Shown are both the total load, and just the unsteady term. The correlation between measurement and calculation is good. The circulatory terms of the ONERA EDLIN and Leishman-Beddoes models are best left out, with the shed wake effects accounted for in the vortex wake model. Without these circulatory terms, the three unsteady aerodynamics models give comparable results.

The correlation between measured and calculated normal force is similar at 95% and 97.8% radius to that at 92% radius. The correlation for pitching moment is fair at 92% radius (figure 8), but worse outboard. The lifting-line wing model of CAMRAD II is second-order for lift, which contributes to the good correlation for lift; but it is still first-order for moments. The measured moments show a variation with radial station at the tip that is probably associated with three-dimensional aerodynamics. The angle of attack varies radially at the tip, but is small enough so at these Mach numbers (effectively reduced by the tip sweep) the static pitch moment is zero (the airfoil is symmetric). Thus the calculated pitching moment consists

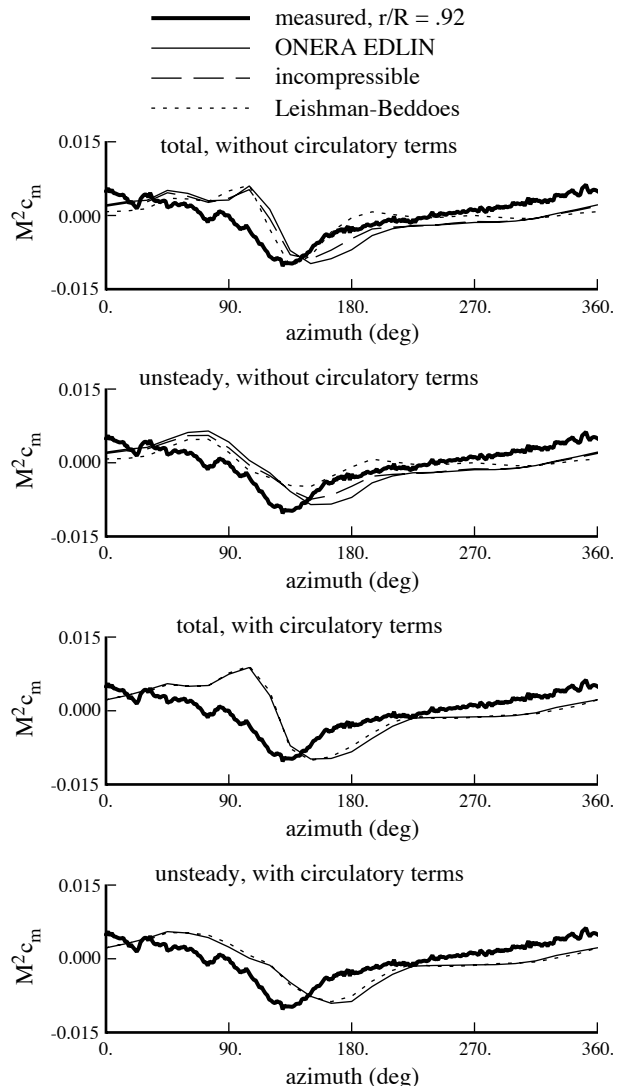


Figure 8. Flight test of Puma with swept tip rotor blade, at $\mu = .38$, $M_{at} = .86$, and $C_T/\sigma = .080$; total section moment and unsteady moment.

primarily of the noncirculatory, unsteady term (figure 8), which does not vary much with tip span station.

The McDonnell Douglas Advanced Bearingless Rotor (MDART) was tested in the NASA Ames Research Center 40- by 80-Foot Wind Tunnel (refs. 27 and 28). Nearly identical results for calculated lag damping and blade loads were obtained using the three unsteady aerodynamics models. The unsteady loads are essential for the analysis, since they provide the blade pitch damping.

A Lynx hingeless-rotor helicopter was flight tested by Westland Helicopters up to and beyond the stall boundary (ref. 29). The flight test included speed sweeps at low and high gross weight, extending into regimes with significant dynamic stall. Figure 9 compares the measured power with

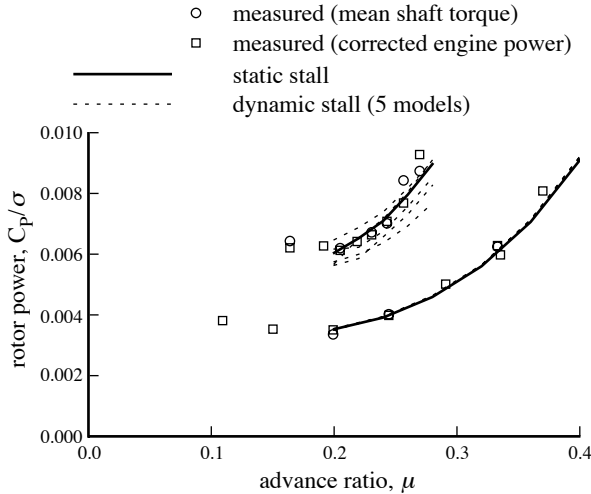


Figure 9. Lynx flight test, at weight $C_T/\sigma = .07$ and $.11$; rotor power (no blade lag or torsion motion).

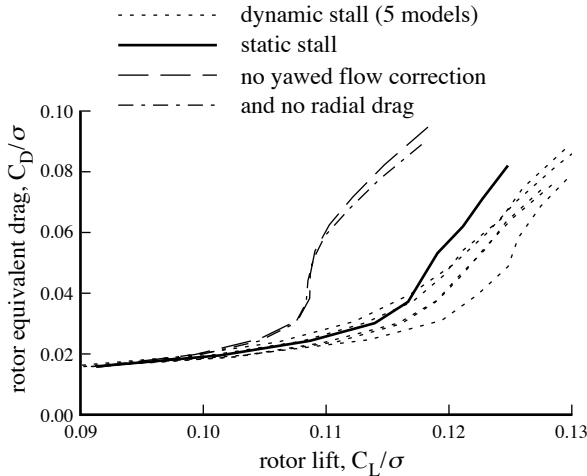


Figure 10. Lynx rotor, at $\mu = .25$ and shaft angle of attack -4 deg; influence of aerodynamic model on calculated rotor drag (no blade lag or torsion motion).

calculations using the five dynamic stall models. This figure is just a reality check rather than correlation, since the calculations were performed without elastic lag or torsion motion of the blades (to isolate the effects of the different aerodynamic models), and because the static airfoil data were not measured much beyond the onset of stall. Figure 10 shows the influence of the aerodynamic model on the calculated rotor drag as a function of rotor lift. Calculations are presented using the five dynamic stall models, as well as with and without the yawed flow corrections. This is not a new result (see ref. 30), except for the presence of five dynamic stall models instead of just one. But figure 10 captures the state-of-the-art well: the effects of yawed flow and dynamic stall are extremely

important in rotor performance, yet their calculation in practical analyses must rely on empirical models.

Free Wake Geometry

The rotor vortex wake is an important factor in most problems of helicopters, including poor performance, high blade loads, high vibration, and high noise levels. An accurate calculation of the wake-induced nonuniform inflow and the resulting blade airloads is needed in order to predict rotor behavior. Below an advance ratio of about $\mu = 0.20$, blade-vortex interaction is particularly strong and therefore an accurate wake geometry is needed as well. The general free wake geometry calculation for wings and rotors that is implemented in CAMRAD II was described in reference 31. The method gave good performance and airloads correlation at advance ratios of 0.05 and above, with reasonable computation speed. The wake geometry distortion can be calculated for multiple wings, multiple rotors, and non-identical blades; for all wake structures, including multiple rolled-up trailed vorticity and inboard sheets as well as tip vortices; using the same wake model as the induced velocity calculations; for transients as well as the trim solution.

Recent developments have extended this free wake method to include hover and ground effect. Application to hover required improvements in the wake geometry extrapolation method, and a model for the tip vortex formation process (initial radial contraction and initial vertical convection). Both for convergence in hover and for efficiency, the capability to require the distortion to be identical for different wings (perhaps with a time shift) is needed. The influence of the ground was introduced by using image vortex elements in the wake geometry and induced velocity calculations. These developments are documented here.

The distortion is evaluated at time t and wake age τ , and may be required at an age beyond which it has been calculated. The time and age increment in the wake geometry calculation is Δt . Let τ_{last} be the maximum age of the available distortion. The distortion is extrapolated by assuming that the vortex element is convected for the time interval $(\tau - \tau_{last})$ by a constant velocity:

$$D(t, \tau) = D(t - (\tau - \tau_{last}), \tau_{last}) + (\tau - \tau_{last}) v_{conv}$$

The distortion is used at a constant value of $(t - \tau)$, which is the time when the wake element was created. The free distortion is calculated for wake ages up to τ_{max} . The accuracy of the wake geometry is generally improved by not using the last part of the calculated distortion, hence starting the extrapolation at τ_{last} less than τ_{max} . Typically the last revolution of the calculated distortion is not used in the extrapolation, particularly for hover and

low advance ratio. Extrapolation uses the convection velocity v_{conv} , obtained from the average distortion increment at τ_{last} :

$$v_{\text{conv}} = \frac{1}{T} \sum_t (D(t, \tau_{\text{last}}) - D(t-\Delta t, \tau_{\text{last}}-\Delta t)) \frac{1}{\Delta t}$$

(in inertial axes, for each distorted structure). This convection velocity is recalculated at the end of each revolution of the wake geometry algorithm, and the final value is saved for use when the wake geometry is evaluated. Optionally, the convection velocity from the rigid or prescribed model can be used to extrapolate the free distortion. For the transient task, the velocity is filtered over the latest period; or the trim convection velocity can be used.

A subset of the wings can have identical trim distortion (in an appropriate frame, with a time shift). Then it is only necessary to calculate the distortion for one wing of the subset (the parent wing). The distortion of the child wing is evaluated from the parent:

$$D_{\text{child}}(t_{\text{child}}, \tau) = D_{\text{parent}}(t_{\text{parent}}, \tau)$$

where $t_{\text{parent}} = t_{\text{child}} + l_{\text{shift}}\Delta t$, and l_{shift} is an input time shift. For example, with N blades uniformly spaced over the period $T = J \Delta t$, the time shift for the m -th blade is $l_{\text{shift}} = (m/N)J$ (which is an integer if J is a multiple of N). If l_{shift} is not an integer, then the parent distortion is interpolated over t and $(t-\tau)$ to obtain the child distortion.

The tip vortex forms on the generating wing at a span station inboard of the wing tip. The location of the tip vortex at the trailing edge can influence the loading and near wake. This effect is implemented in the wing component, by assuming that the bound circulation is zero outboard of the location of the tip vortex at the trailing edge. For a highly tapered wing tip, the tip vortex can form 4–6% span inboard of the tip, and the effect on the loading is significant. For a rectangular planform, the effect is small and can be ignored. Further entrainment occurs in the wake, so the tip vortex effectively forms at an initial span station r_{TV} inboard of the tip. The wake geometry components implement the effect of this initial contraction by assuming that the tip vortices and sheet edges are described by trailed lines arising from span stations r_{TV} rather than from the tips. In the wake geometry components, r_{TV} is an input parameter, or it is calculated assuming that the centroid of the trailed vorticity is conserved (Betz rollup).

The initial span station of the tip vortex can be obtained from Betz rollup as follows. Consider the bound vorticity from r_A to r_B , rolling up into a trailed line. The centroid of the trailed vorticity is at r_C :

$$\begin{aligned} r_C (\Gamma_A - \Gamma_B) &= \int_{r_A}^{r_B} \frac{\partial \Gamma}{\partial r} r \, dr = \Gamma_B r_B - \Gamma_A r_A - \int_{r_A}^{r_B} \Gamma \, dr \\ &= \Gamma_B r_B - \Gamma_A r_A - (r_A - r_B) \Gamma_M \end{aligned}$$

in terms of the mean bound circulation Γ_M ; hence

$$r_C = (1-w) r_A + w r_B$$

with $w = (\Gamma_M - \Gamma_B) / (\Gamma_A - \Gamma_B)$. The spanwise displacement calculated by the Betz rollup model is multiplied by an input factor; and for the wing tips, added to the input displacement. At the wing tips, it is assumed that the vorticity that rolls up is between the nearest bound circulation peak and the tip. At inboard stations, it is assumed that the vorticity that rolls up is between the nearest peak in the panel to the left and the nearest peak in the panel to the right. With the single-peak wake model, this peak is at the maximum bound circulation; with dual peaks in the circulation distribution, the right or left peak is used. The mean bound circulation Γ_M is evaluated assuming piecewise-linear variation of the bound circulation over the span.

With a three-dimensional wing, the Kutta condition requires that the wake leave the trailing-edge tangent to the wing surface (ref. 32). In the absence of a calculation of the detailed flow field near the wing, this requirement can be satisfied by using an initial convection velocity $q_K = \Gamma / \pi c$, where Γ is the section bound circulation and c is the chord. This result is obtained using the zero-lift chord line for the trailing-edge bisector, and a lift-curve slope of 2π . The velocity direction is assumed to be perpendicular to the plane defined by the bound vortex and the trailed vortex element to the collocation point. The initial velocity q_K is used for collocation points at wake age $\tau = 0$, and the actual wake self-induced velocity q at age $\tau \geq \tau_K$, so

$$(1 - \tau/\tau_K) q_K + (\tau/\tau_K) q$$

replaces q for $\tau < \tau_K$. The age τ_K must be selected based on correlation with measured wake geometry and performance. Optionally this initial convection velocity can be ignored (q_K never replacing q). Hover performance calculations require $\tau_K > 0$, but in forward flight best results are obtained with a much smaller value of τ_K . Thus for hover, the initial convection velocities are defined such that the wake leaves the wing tangent to the wing surface. The EHPIC analysis (refs. 33 and 34) has a similar feature, implemented differently: the first element of the trailing vortices is constrained to leave the rotor blade parallel to the lifting surface.

Generally it is only the distorted geometry of the tip vortices that is calculated. Prescribed geometry can be used for the inboard vorticity sheets.

Table 1. Tip vortex formation in hover.

rotor	UH-60A	tapered	rect.	ogee	S-76	XV-15		
number of blades	4	4	2	2	4	3		
radius R (ft)	4.683	4.683	3.43	3.43	3.5	12.5		
solidity σ	.0825	.0825	.0464	.0396	.0748	.089		
chord c/R or c_{tip}/R	.065	.022	.073	.073	.059	.093		
$2.5(c/R \text{ or } c_{tip}/R)$.16	.05	.18	.18	.15	.23		
τ_K	.15	.05	.15	.15	.15	.23		
prescribed r_{TV}	.99	.97	.96	.91	.99	.98		
Betz rollup r_{TV}	r_{Betz}	$r_{Betz}^{-.01}$	$r_{Betz}^{-.02}$	$r_{Betz}^{-.02}$	r_{Betz}	$.4r_{Betz}$		
wake geometry at first encounter with following blade (vertical convection z/R and radial contraction r/R)								
C_T/σ	.0856	.1069	.0773	.1014	.099	.103	.078	.1018
measured z/R	.0285±.005	.0405±.005	.013±.005	.022±.005	.065	.069	.045±.015	.060±.015
prescribed	.030	.046	.009	.019	.066	.070	.027	.067
Betz rollup	.029	.047	.012	.020	.065	.070	.029	.068
measured r/R	.925±.007	.921±.007	.907±.007	.907±.007	.865	.820	.915±.015	.890±.015
prescribed	.946	.940	.915	.908	.867	.824	.947	.918
Betz rollup	.948	.938	.912	.905	.870	.821	.943	.916

The influence of the ground can be included in the wake-induced velocity calculation and in the wake geometry calculation, through the use of image elements in the wake model. For inviscid flow, the boundary condition imposed by the ground is zero normal wake-induced velocity at the ground plane. This constraint is satisfied by introducing an image element for every vortex element in the wake model. The image element is created from the vortex element by changing the sign of the strength, and reflecting the position across the ground plane. A wake element can be too near or below the ground plane. This can occur with rigid or prescribed geometry that does not include the effect of the ground; or because of numerical effects in the free geometry calculation. Here "near" the ground plane is defined by a distance δ above ground level (δ could be zero or even negative). Optionally, the analysis neglects any part of a vortex element (and the corresponding part of the image) that is below the height δ . It is found that the solution for the distortion places the wake elements completely above the ground plane (as long as the elements are not too long). Thus this feature improves convergence of the distortion calculation, without actually affecting the position of the distorted elements above the ground plane.

With this inviscid and steady free wake geometry, it is an idealized problem that is solved, not the actual viscous and unsteady flow field of a hovering rotor. So the objective of a consistent and reliable calculation of hover

performance can be achieved only on the basis of correlation with measured wake geometry, airloads, and performance. Progress in the analysis of hovering rotors is here measured by a narrowing focus of empiricism: from a factor on the uniform induced-velocity for momentum theory; to parameters defining the wake geometry for prescribed methods; to the initial convection and initial contraction, wake extent, and core size for free wake methods based on inviscid aerodynamics.

Hover Correlation

Figure 11 shows an example of the calculated free wake geometry in hover. Figure 12 shows the calculated wake geometry in ground effect; the advance ratio is $\mu = .02$, and the height of the hub above the ground is 50% the rotor diameter.

The tip vortex formation process (initial radial contraction and initial vertical convection) was calibrated using measured wake geometry at the first encounter with a following blade, and measured blade airloads. Table 1 summarizes the results. The required extent of the initial convection is approximately $\tau_K = 2.5c/R$ revolutions, which is typically about 0.15 revolutions. With taper over a large span range, the tip chord should be used to estimate τ_K . The initial span station r_{TV} depends on blade number (table 1 shows $r_{TV} = .99R, .98R, .96R$ for 4, 3, 2 blades respectively) and on planform taper. Betz rollup typically

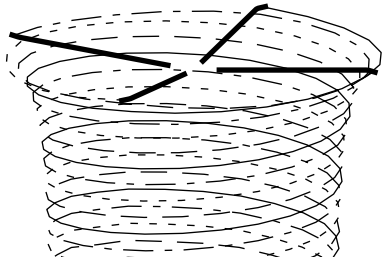


Figure 11. Calculated hover wake geometry (S-76 rotor at $C_T/\sigma = .08$).

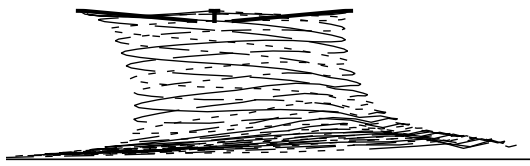


Figure 12. Calculated free wake geometry in ground effect (S-76 rotor at $C_T/\sigma = .08$, $\mu = .02$, height above ground = 50% rotor diameter).

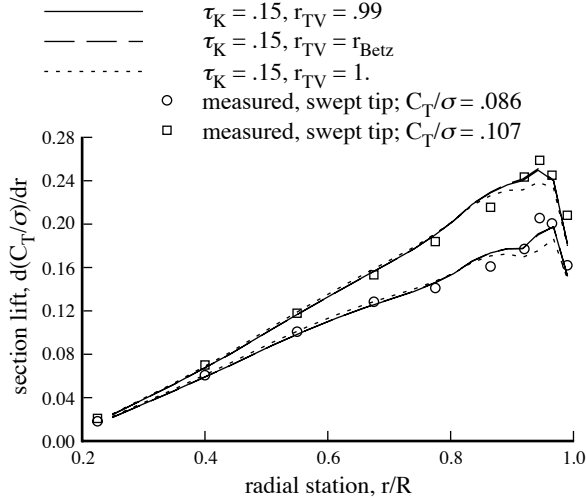


Figure 13. Blade section lift in hover for model UH-60A rotor ($C_T/\sigma = .086$ and $.107$, $M_{tip} = .63$).

requires an additive or multiplicative correction, but has the advantage that it can be easily applied to multiple rollup cases. These results for r_{TV} give good correlation for the tip loading, although in some cases the measured wake geometry at the first encounter with a following blade is perhaps $.02R$ further inboard than the calculated position.

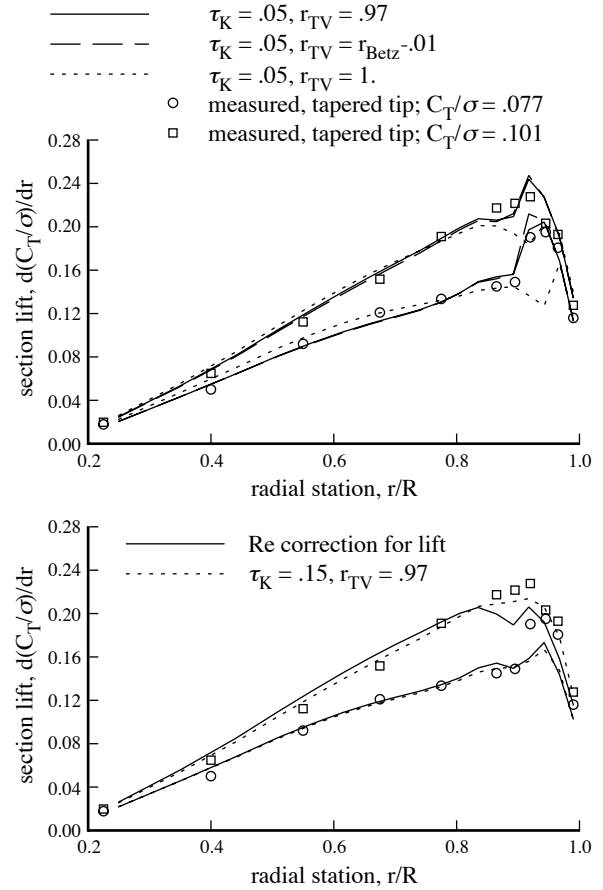


Figure 14. Blade section lift in hover for model tapered rotor ($C_T/\sigma = .077$ and $.101$, $M_{tip} = .63$).

Figures 13 to 15 compare the calculated loading and wake geometry with measurements on a 1/5.73-scale model UH-60A rotor and a corresponding tapered-tip rotor (refs. 35 to 37). The UH-60A model had a 20-deg swept tip beginning at $.93R$, and approximately the full-scale UH-60 twist distribution. The tapered model had 1:3 taper beginning at $.82R$, no sweep, and linear twist. The cases shown are those presented in reference 37. A Reynolds number correction has been applied to the drag coefficient (based on a 1/5-th power scaling of the drag), but not to the maximum lift. Figure 13 shows the loading for the UH-60A. A $.01R$ inboard shift of the initial span station of the tip vortex gives a small improvement of the peak loading calculation. Figure 14 shows the loading for the tapered tip. A $.03R$ inboard shift of the initial span station of the tip vortex gives a significant improvement of the peak loading calculation; and the extent of the initial convection scales with the tip chord in this case. Applying the Reynolds number correction to the maximum lift does not give the correct peak loading. Figure 15 compares the calculated wake geometry with vertical and radial positions measured at the first encounter with a following blade.

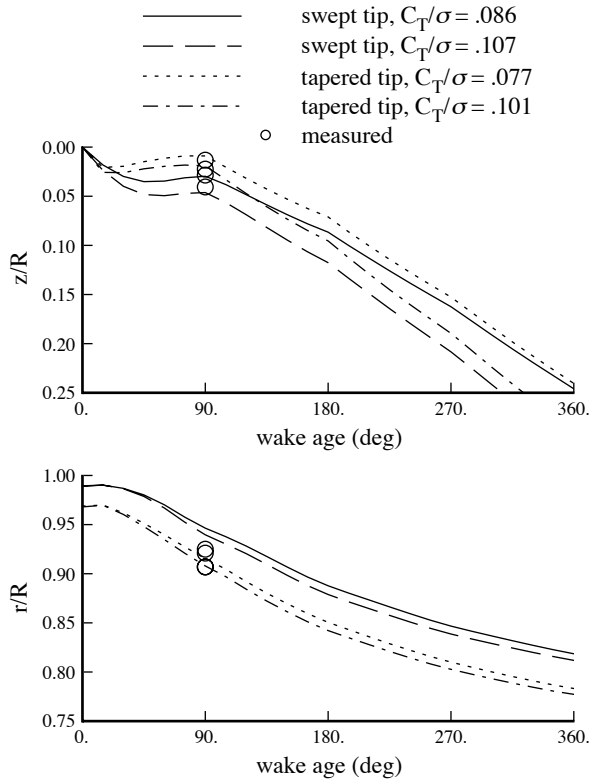


Figure 15. Hover wake geometry for model UH-60A and tapered rotors (vertical convection z/R and radial contraction r/R).

Figures 16 and 17 compare the calculated circulation and wake geometry with measurements on a model two-bladed rotor, for rectangular and ogee tip planforms (ref. 38). A $.04R$ inboard shift of the initial span station of the tip vortex gives an improvement of the peak circulation calculation. Note that for the ogee tip, the blade lift and circulation are suppressed outboard of $.95R$; the measurements showed near the blade trailing edge the tip vortex forming at about $.94R$. Figure 17 compares the calculated wake geometry with the vertical and radial positions measured at the first encounter with a following blade. Figure 17 includes results for the S-76 and XV-15 rotors as well; the measured data are from references 39 and 40 respectively.

Figures 18 to 22 compare measured hover performance with free wake geometry calculations for several rotors. Power is presented instead of figure of merit for the usual reason: the correlation appears much better. Figure 18 shows the performance of the 1/5.73-scale model UH-60A rotor and the tapered-tip rotor; the measured performance data are from references 36 and 37. Figures 19 and 20 show the performance of the S-76 and Bo-105 rotors. The measured data are from references 41 and 42 respectively. The calculations do not show a large effect of blade elastic

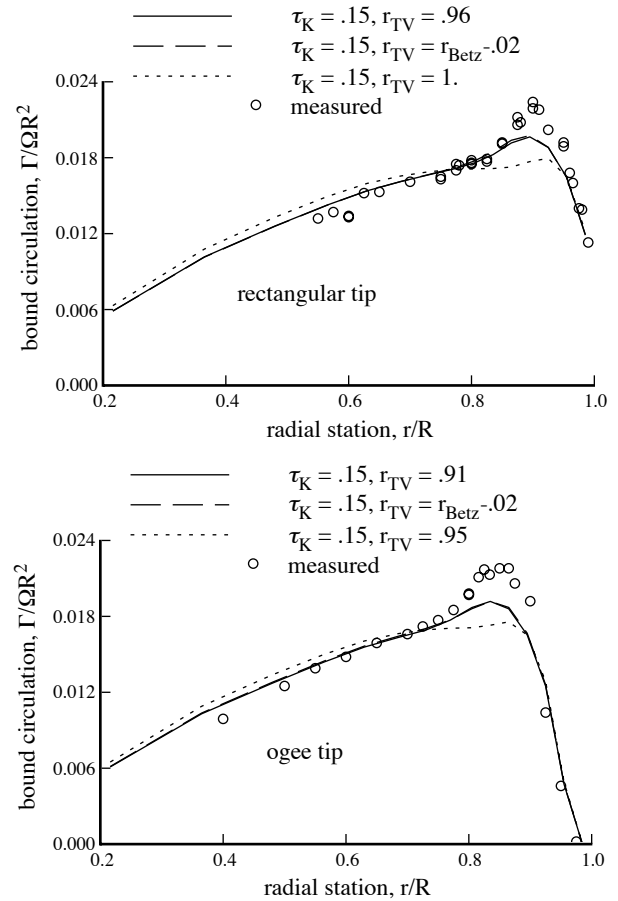


Figure 16. Blade bound circulation in hover for model rotors with rectangular and ogee tip planforms ($C_T/\sigma = .099$ and $.103$, $M_{tip} = .22$).

motion. Figure 21 shows the performance of the AH-64 and UH-60 rotors. The aircraft performance was measured in flight by the USAAEFA (refs. 43 and 44); the data were corrected to just main rotor performance by Baserga and Scully of the USAATCOM (ref. 45). The calculated performance is improved for the AH-64 using an elastic instead of a rigid blade model. Figure 22 shows the performance of the XV-15 rotor. The measured data are from reference 46.

The measured hover performance and wake geometry of the XV-15 rotor with a subwing are presented in references 47 and 40. The subwings had approximately 6 inch span and 3 inch chord; and were tested at high and low incidence relative the tip. Figures 23 and 24 show the calculated wake geometry with the subwing; and figure 25 compares the measured and calculated performance, with and without the subwing. All the normalized results in figures 24 and 25 are based on the radius and solidity of the blade without the subwing. The geometry of the primary tip vortex and the influence of the subwings on the rotor performance are

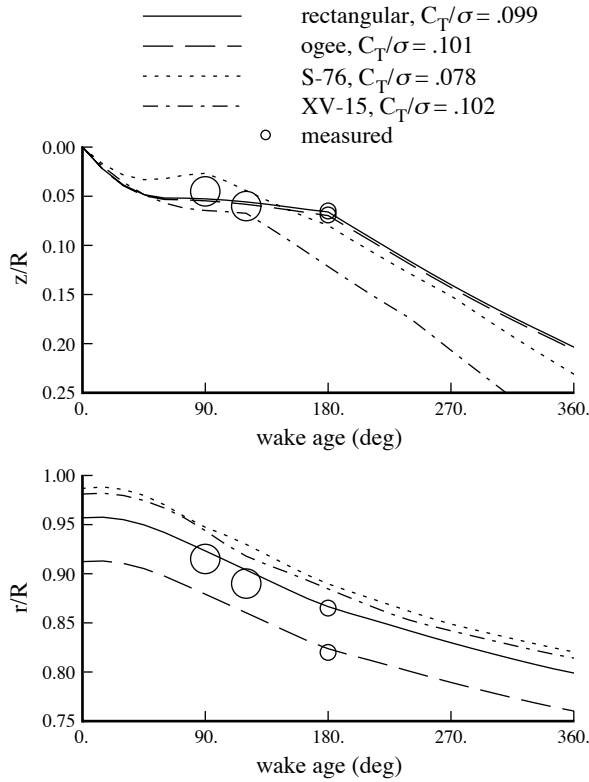


Figure 17. Hover wake geometry for model rotors with rectangular and ogee tip planforms, model S-76 rotor, and full scale XV-15 rotor (vertical convection z/R and radial contraction r/R).

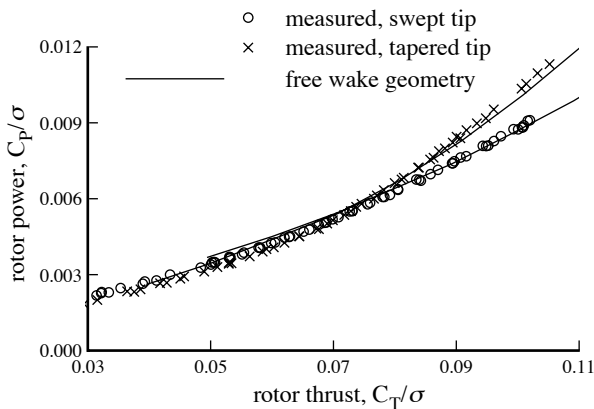


Figure 18. Hover performance of model UH-60A and tapered rotors ($M_{tip} = .63$).

calculated reasonably well. In this thrust range, the performance calculations without the subwing compare well with the OARF test data (ref. 46, see figure 22), while the wind tunnel measurements (ref. 47) show somewhat higher power. So it is the change in the power produced by the subwings that should be compared in figure 25. Figure 24 shows the influence of rollup model,

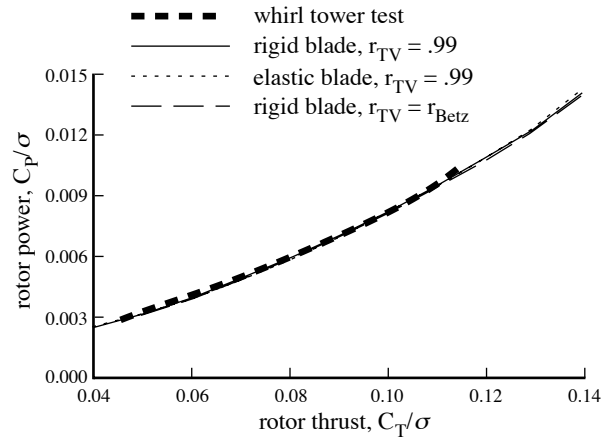


Figure 19. Hover performance of S-76 rotor ($M_{tip} = .605$).

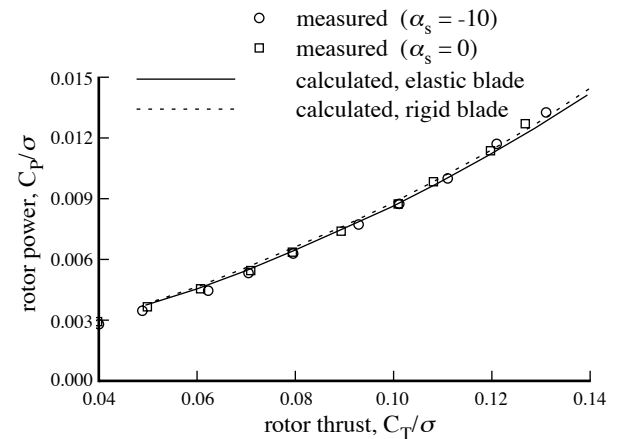


Figure 20. Hover performance of Bo-105 rotor ($M_{tip} = .65$).

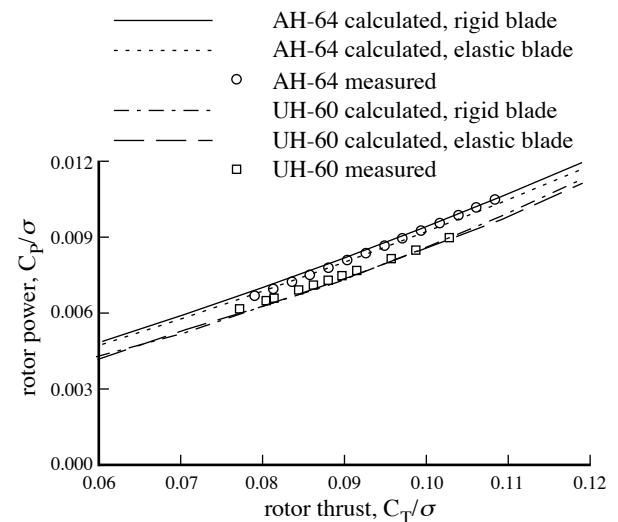


Figure 21. Hover performance of AH-64 and UH-60 rotors (measured performance derived from flight tests).

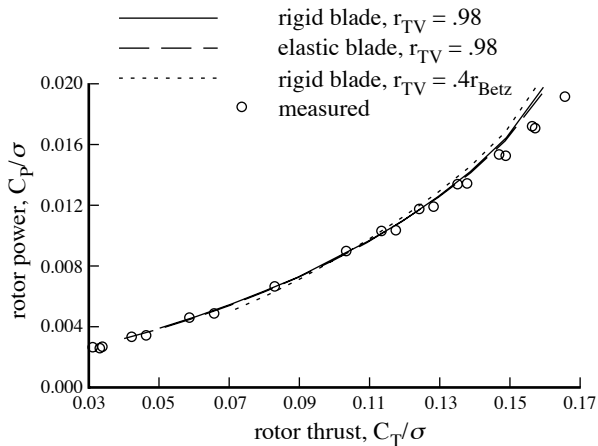


Figure 22. Hover performance of XV-15 rotor ($M_{tip} = .69$).

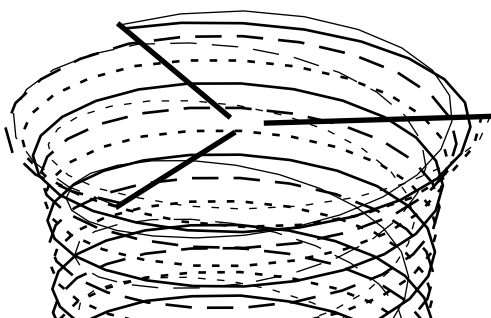


Figure 23. Calculated hover wake geometry for XV-15 rotor with subwing ($C_T/\sigma = .102$, $M_{tip} = .69$).

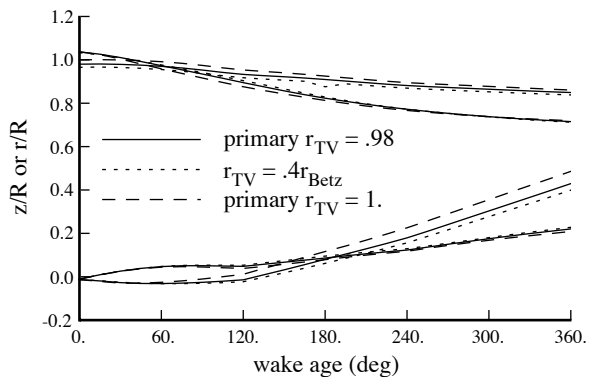


Figure 24. Influence of rollup model on calculated hover wake geometry of XV-15 rotor with subwing, at $C_T/\sigma = .102$ (vertical convection z/R and radial contraction r/R).

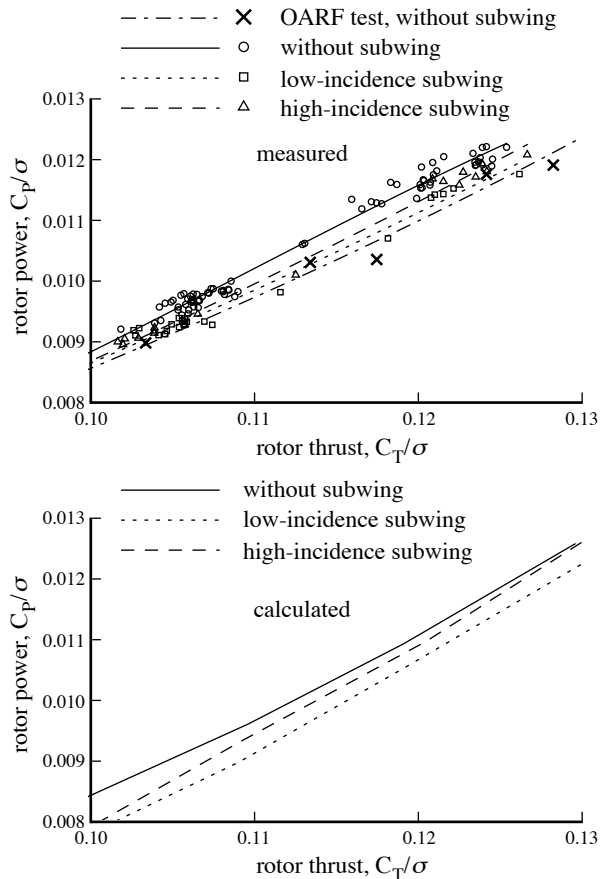


Figure 25. Hover performance of XV-15 rotor with and without subwing ($M_{tip} = .69$).

specifically the initial span station. The calculations produce 90 deg rotation of the subwing vortex about the primary vortex at wake ages between 35 and 90 deg, depending on the rollup model; the measurements show 90 deg rotation at about 45 deg wake age (ref. 40). Thereafter the calculated subwing vortex does not rotate about the primary vortex as fast as measured: 180 deg rotation is found at 140 to 210 deg wake age, instead of at 75 deg wake age as measured. This difference reflects the absence of a model of the entrainment and combination of the subwing and primary vortex into a single vortex, as observed in the measurements.

Concluding Remarks

Recent developments of the aerodynamics models for the comprehensive analysis CAMRAD II have been described, specifically the unsteady aerodynamic models and dynamic stall models. Three models for the unsteady aerodynamic loads in attached flow are implemented: from incompressible thin-airfoil theory, from ONERA EDLIN, and from Leishman-Beddoes. Five dynamic stall models are

implemented: from Johnson, Boeing, Leishman-Beddoes, ONERA EDLIN, and ONERA BH.

For attached flow unsteady aerodynamics, the ONERA EDLIN and Leishman-Beddoes models are approximations to the results of compressible thin-airfoil theory. They give comparable results for calculations of rotor behavior. Care must be taken with a vortex wake or dynamic inflow model that the shed wake effects are neither omitted nor duplicated. Correlation with the Puma measured airloads shows that the circulatory terms of these theories are best left out, with the shed wake effects accounted for in the vortex wake model. Without the circulatory term, the ONERA EDLIN model is simplest, just introducing factors that are functions of Mach number, without any state equations. These factors give a good representation of Küssner's coefficients, except that the moment produced by heave is always real, when it should exhibit a phase shift for nonzero Mach number. The Leishman-Beddoes method seems to offer a sounder basis for approximating the loads, and it may be possible to use a quasistatic solution for the impulsive terms. While giving nonsingular results at zero Mach number, this theory does not however include the incompressible limit exactly.

The dynamic stall models have been revised as required to use the airfoil tables for steady characteristics (evaluated at an angle of attack that includes the dynamic stall delay). Retaining the use of airfoil table data is considered essential, both to provide the basic characteristics associated with airfoil shape, and to isolate the effects of the dynamic stall model. Among the dynamic stall models, the Boeing model is the simplest, requiring only three parameters. However, the Boeing model does not include the loads produced by the leading-edge vortex; and the form of the angle of attack delay is much different from that of the other models. The ONERA EDLIN and ONERA BH models require a large number of parameters. The Leishman-Beddoes model is attractive because the parameters defining trailing-edge separation point and critical lift coefficient are obtained from the static airfoil characteristics. However, the time constants required by the Leishman-Beddoes model do not seem to have universal values, but depend on the airfoil shape. The differences obtained using these dynamic stall models are no more than should be expected from empirical methods. The correlation for the oscillating three-dimensional wing may be judged remarkably good considering the simplicity of some of the models; and also exhibiting significant errors, as expected with empirical models. There is a very large effect of the dynamic stall model as well as yawed flow corrections on calculated rotor performance in extreme operating conditions, yet their calculation in practical analyses must rely on empirical models.

Recent developments have extended the CAMRAD II free wake method to include hover and ground effect. Application to hover required improvements in the wake geometry extrapolation method; a model for the tip vortex formation process (initial radial contraction and initial vertical convection); and the capability to require the distortion to be identical for different wings. A model for the tip vortex formation is required in the absence of detailed calculations of the flow field at the wing tip and near wake. Such detailed calculations are much needed. With this inviscid and steady free wake geometry, it is an idealized problem that is solved, not the actual viscous and unsteady flow field of a hovering rotor. Correlation with measured wake geometry, airloads, and performance has demonstrated the capability to calculate hover performance.

References

- 1) Johnson, W. "CAMRAD II, Comprehensive Analytical Model of Rotorcraft Aerodynamics and Dynamics." Johnson Aeronautics, Palo Alto, California, 1992-1997.
- 2) Johnson, W. "Technology Drivers in the Development of CAMRAD II." American Helicopter Society, Aeromechanics Specialists Meeting, San Francisco, January 1994.
- 3) Johnson, W. Helicopter Theory. Princeton University Press, Princeton, New Jersey, 1980.
- 4) Küssner, H.G., and Schwarz, L. "The Oscillating Wing with Aerodynamically Balanced Elevator." NACA TM 991, October 1941.
- 5) Theodorsen, T., and Garrick, I.E. "Nonstationary Flow About a Wing-Aileron-Tab Combination Including Aerodynamic Balance." NACA Report 736, 1942.
- 6) Petot, D. "Differential Equation Modeling of Dynamic Stall." La Recherche Aerospaciale, Number 1989-5 (corrections dated October 1990).
- 7) Peters, D. "Toward a Unified Lift Model for Use in Rotor Blade Stability Analyses." Journal of the American Helicopter Society, Volume 30, Number 3, July 1985.
- 8) Barwey, D.; Gaonkar, G.H.; and Ormiston, R.A. "Investigation of Dynamic Stall Effects on Isolated Rotor Flap-Lag Stability with Experimental Correlation." Journal of the American Helicopter Society, Volume 36, Number 4, October 1991.
- 9) Barwey, D., and Gaonkar, G.H. "Dynamic-Stall and Structural-Modeling Effects on Helicopter Blade Stability with Experimental Correlation." AIAA Journal, Volume 32, Number 4, April 1994.
- 10) van der Vooren, A.I. "The Theodorsen Circulation Function and Aerodynamic Coefficients." AGARD Manual on Aeroelasticity, Volume VI, January 1964.
- 11) Leishman, J.G. "Validation of Approximate Indicial Aerodynamic Functions for Two-Dimensional Subsonic Flow." Journal of Aircraft, Volume 25, Number 10, October 1988.
- 12) Hariharan, N., and Leishman, J.G. "Unsteady Aerodynamics of a Flapped Airfoil in Subsonic Flow by Indicial Concepts." Journal of Aircraft, Volume 33, Number 5, September-October 1996.

- 13) Leishman, J.G., and Nguyen, K.Q. "State-Space Representation of Unsteady Airfoil Behavior." *AIAA Journal*, Volume 28, Number 5, May 1990.
- 14) Johnson, W. "The response and Airloding of Helicopter Rotor Blades Due to Dynamic Stall." Massachusetts Institute of Technology, ASRL TR 130-1, May 1970.
- 15) McCroskey, W.J. "Recent Developments in Dynamic Stall." Symposium on Unsteady Aerodynamics, Tucson, Arizona, March 1975.
- 16) Beddoes, T.S. "A Synthesis of Unsteady Aerodynamic Effects Including Stall Hysteresis." *Vertica*, Volume 1, Number 2, 1976.
- 17) Ham, N.D., and Garelick, M.S. "Dynamic Stall Considerations in Helicopter Rotors." *Journal of the American Helicopter Society*, Volume 13, Number 2, April 1968.
- 18) Harris, F.D.; Tarzanin, F.J., Jr., and Fisher, R.K., Jr. "Rotor High Speed Performance, Theory vs. Test." *Journal of the American Helicopter Society*, Volume 15, Number 3, April 1970.
- 19) Tarzanin, F.J., Jr. "Prediction of Control Loads Due to Blade Stall." *Journal of the American Helicopter Society*, Volume 17, Number 2, April 1972.
- 20) Gormont, R.E. "A Mathematical Model of Unsteady Aerodynamics and Radial Flow for Application to Helicopter Rotors." USAAVLABS TR 72-67, May 1973.
- 21) Leishman, J.G., and Beddoes, T.S. "A Semi-Empirical Model for Dynamic Stall." *Journal of the American Helicopter Society*, Volume 24, Number 3, July 1989.
- 22) Leishman, J.G., and Beddoes, T.S. "A Generalized Model for Airfoil Unsteady Aerodynamic Behavior and Dynamic Stall Using the Indicial Method." *American Helicopter Society Forum*, June 1986.
- 23) Leishman, J.G., and Crouse, G.L., Jr. "State-Space Model for Unsteady Airfoil Behavior and Dynamic Stall." *AIAA Paper Number 89-1319*, April 1989.
- 24) Truong, V.K. "A 2-D Dynamic Stall Model Based on a Hopf Bifurcation." *European Rotorcraft Forum*, Italy, September 1993.
- 25) R.A. Piziali, "2-D and 3-D Oscillating Wing Aerodynamics for a Range of Angles of Attack Including Stall." *NASA TM 4632*, September 1994.
- 26) Bousman, W.G.; Young, C.; Gilbert, N.; Toulmay, F.; Johnson, W.; and Riley, M.J. "Correlation of Puma Airloads - Lifting-Line and Wake Calculation." *NASA TM 102212*, November 1989.
- 27) Nguyen, K.; McNulty, M.; Anand, V.; and Lauzon, D. "Aeroelastic Stability of the McDonnell Douglas Advanced Bearingless Rotor." *American Helicopter Society Forum*, May 1993.
- 28) Nguyen, K.; Lauzon, D.; and Anand, V. "Computation of Loads on the McDonnell Douglas Advanced Bearingless Rotor." *American Helicopter Society Forum*, May 1994.
- 29) Lau, B.H.; Louie, A.W.; Sotiriou, C.P.; and Griffiths, N. "Correlation of the Lynx-XZ170 Flight-Test Results Up To and Beyond the Stall Boundary." *American Helicopter Society Forum*, May 1993.
- 30) Harris, F.D.; Tarzanin, F.J., Jr.; and Fisher, R.K., Jr. "Rotor High Speed Performance, Theory vs. Test." *Journal of the American Helicopter Society*, Volume 15, Number 3, July 1970.
- 31) Johnson, W. "A General Free Wake Geometry Calculation for Wings and Rotors." *American Helicopter Society Forum*, May 1995.
- 32) Hess, J.L. "The Problem of Three-Dimensional Lifting Potential Flow and Its Solution by Means of Surface Singularity Distribution." *Computer Methods in Applied Mechanics and Engineering*, Volume 4, Number 3, November 1974.
- 33) Felker, F.F.; Quackenbush, T.R.; Bliss, D.B.; and Light, J.S. "Comparisons of Predicted and Measured Rotor Performance in Hover Using a New Free Wake Analysis." *Vertica*, Vol. 14, No. 3, 1990.
- 34) Quackenbush, T.R.; Bliss, D.B.; Wachspress, D.A.; and Ong, C.C. "Free Wake Analysis of Hover Performance Using a New Influence Coefficient Method." *NASA CR 4309*, July 1990.
- 35) Lorber, P.F.; Stauter, R.C.; and Landgrebe, A.J. "A Comprehensive Hover Test of the Airloads and Airflow of an Extensively Instrumented Model Helicopter Rotor." *American Helicopter Society Forum*, May 1989.
- 36) Tung, C., and Ramachandran, K. "Hover Performance Analysis of Advanced Rotor Blades." *American Helicopter Society Forum*, June 1992.
- 37) Tung, C., and Lee, S. "Evaluation of Hover Performance Prediction Codes." *American Helicopter Society Forum*, May 1994.
- 38) Ballard, J.D.; Orloff, K.L.; and Luebs, A.B. "Effect of Tip Shape on Blade Loading Characteristics and Wake Geometry for a Two-Bladed Rotor in Hover." *Journal of the American Helicopter Society*, Volume 25, Number 1, January 1980.
- 39) Norman, T.R., and Light, J.S. "Rotor Tip Vortex Geometry Measurements Using the Wide-Field Shadowgraph Technique." *Journal of the American Helicopter Society*, Volume 32, Number 2, April 1987.
- 40) Lau, B.H.; Wadcock, A.J.; and Heineck, J.T. "Wake Visualization of a Full-Scale Tilt Rotor in Hover." *AHS Specialists' Meeting for Rotorcraft Acoustics and Aerodynamics*, Williamsburg, Virginia, October 1997.
- 41) Jepson, D.; Moffitt, R.; Kilzinger, K.; and Bissell, J. "Analysis and Correlation of Test Data from an Advanced Technology Rotor System." *NASA CR 3714*, August 1983.
- 42) Peterson, R.L. "Full-Scale Hingeless Rotor Performance and Loads." *NASA TM 110356*, June 1995.
- 43) Picasso, B.D., III; Downs, G.T.; Buckanin, R.M.; and Ottomeyer, J.D. "Airworthiness and Flight Characteristics Test, Part 2, YAH-64 Advanced Attack Helicopter." *USAAEFA Report 80-17-2*, February 1982.
- 44) Nagata, J.I.; Piotrowski, J.L.; Young, C.J.; Lewis, W.D.; Losier, P.W.; and Lyle, J.A. "Baseline Performance Verification of the 12th Year Production UH-60A Black Hawk Helicopter." *USAAEFA Report 87-32*, January 1989.
- 45) Baserga, C. "Rotor/Propeller Axial Flight Performance Model." *Advanced System Research and Analysis Office, USAATCOM, Moffett Field, California*, April 1994.
- 46) Felker, F.F.; Betzina, M.D.; and Signor, D.B. "Performance and Loads Data from a Hover Test of a Full-Scale XV-15 Rotor." *NASA TM 86833*, November 1985.
- 47) Light, J.S. "Results From an XV-15 Rotor Test in the National Full-Scale Aerodynamics Complex." *American Helicopter Society Forum*, May 1997.

APPENDIX A: Unsteady Airfoil Motion

This appendix presents the equations for the unsteady aerodynamics models of CAMRAD II. Models from incompressible thin-airfoil theory, ONERA EDLIN, and Leishman-Beddoes are implemented. The unsteady loads depend on the upwash w (the normal velocity of the wing relative to the air, measured at the quarter chord), and the upwash gradient along the chord $w' = \partial w / \partial x$ (typically from a pitch rate). In the equations below, U is the resultant velocity of the airfoil section (always positive); V is chordwise velocity of the wing relative the air (negative in reverse flow); M is the section Mach number; and c is the chord. When implemented, the appropriate changes in reverse flow are included.

Incompressible Thin-Airfoil Theory

The incompressible unsteady loads are derived following reference 3. In coefficient form, the results for unsteady circulation, lift, and moment are:

$$\begin{aligned} c_{gUS} &= \frac{a}{U} \left[w' \frac{c}{2} \right] \\ c_{\ell US} &= \frac{a}{U^2} \left[V w' \frac{c}{2} + \frac{c}{4} \left(\dot{w} + \frac{c}{4} \dot{w}' \right) \right] \\ c_{m US} &= (x_{AF} - x_{AC}) c_{\ell US} + \frac{a}{U^2} \left[-V w' \frac{c}{16} - \frac{c}{16} \left(\dot{w} + \frac{3c}{8} \dot{w}' \right) \right] \end{aligned}$$

The following options are implemented for the lift-curve slope a : (1) constant; (2) Prandtl-Glauert; (3) Prandtl-Glauert with lift divergence; (4) from the airfoil table at zero lift; (5) from the airfoil table at the local angle of attack; (6) secant slope from the airfoil table. Different choices can be made for the circulatory lift, other lift, and moment. According to steady thin-airfoil theory, both the lift and moment scale with the Prandtl-Glauert factor. The following options are implemented for the aerodynamic center shift $\delta x = x_{AF} - x_{AC}$: (1) constant; (2) from the airfoil table at zero lift; (3) from the airfoil table at the local angle of attack. Here x_{AF} is the position of the reference axis of the airfoil coefficients, and x_{AC} is the position of the actual aerodynamic center; both measured as fraction of the chord aft of the leading edge (usually $x_{AF} = .25$). These several choices for a and δx are needed to accommodate the aerodynamic theories as originally developed.

ONERA EDLIN Theory

The ONERA EDLIN (Equations Differentielles Lineaires) theory for the unsteady loads is presented in reference 6. To include the effects of compressibility, Küssner's coefficients are used, as tabulated by van der Vooren (ref. 10) and curve-fit by Petot (ref. 6). In coefficient form, the results are:

$$\begin{aligned} c_{\ell US} &= \frac{a}{U^2} \left[V w' \frac{c}{2} + \frac{c}{4} \left(\dot{w} f_{L0} + \frac{c}{4} \dot{w}' f_{L1} \right) \right] + \frac{a}{U} L_1 & c_{gUS} &= \frac{a}{U} \left[w' \frac{c}{2} \right] + \frac{a}{U} L_1 \\ c_{m US} &= (x_{AF} - x_{AC}) c_{\ell US} + \frac{a}{U^2} \left[-V w' \frac{c}{16} f_{M0} - \frac{c}{16} \left(\dot{w} f_{M0} + \frac{3c}{8} \dot{w}' f_{M1} \right) \right] & \dot{L}_1 + \lambda L_1 &= \mu \left[\dot{w} + \dot{w}' \frac{c}{2} \right] \end{aligned}$$

where $f_{L0} = \beta[1 + 5(\beta^{.57} - 1)]$, $f_{L1} = \beta[1 + 3.92(\beta - 1)]$, $f_{M0} = \beta[1 + 1.4M^2]$, $f_{M1} = \beta[-1.2625 + 1.5330 \tan^{-1}(10.5 - 15M)]$; and $\beta = \sqrt{1 - M^2}$. These factors give a good representation of Küssner's coefficients, except that the moment produced by heave ($c_{m_h} = \frac{\pi}{4} k^2 f_{M0}$) is always real, when it should exhibit a phase shift for $M > 0$. The L_1 term accounts for the airfoil shed wake effects (lift deficiency function), with $\lambda = (2U/c)\lambda_0(1 - .76M)$ and $\mu = -\frac{1}{4}(3 - \beta)$. Petot (ref. 6) gives a value of 0.17 for λ_0 . The ONERA EDLIN theory as presented by Petot (ref. 6) uses the Prandtl-Glauert option for the lift-curve slope a . The ONERA BH theory (ref. 24) implies using the lift-curve slope at the local angle of attack.

Leishman-Beddoes Theory

The Leishman-Beddoes theory for unsteady loads in attached flow is presented in references 11 to 13. In coefficient form, the results are:

$$c_{g_{US}} = \frac{a}{U} (L_{C1} + L_{C2})$$

$$c_{\ell_{US}} = \frac{a}{U} (L_{C1} + L_{C2}) + \frac{a\beta}{U^2} \left[c c_{0\alpha} k_\alpha L_\alpha + c^2 c_{0q} k_q L_q \right]$$

$$\dot{L}_{C1} + \lambda_1 L_{C1} = \lambda_1 A_1 c_{\infty q} c w' - A_1 c_{\infty \alpha} \dot{w} \qquad \dot{L}_\alpha + \lambda_\alpha L_\alpha = \lambda_\alpha \dot{w}$$

$$\dot{L}_{C2} + \lambda_2 L_{C2} = \lambda_2 A_2 c_{\infty q} c w' - A_2 c_{\infty \alpha} \dot{w} \qquad \dot{L}_q + \lambda_q L_q = \lambda_q \dot{w}'$$

$$\lambda_1 = (2U/c) b_1 \beta^2 \qquad \lambda_2 = (2U/c) b_2 \beta^2$$

$$\lambda_\alpha = U/(cMk_\alpha) \qquad \lambda_q = U/(cMk_q)$$

$$c_{m_{US}} = (x_{AF} - x_{AC}) c_{\ell_{US}} + \frac{a}{U} M_{C1} + \frac{a\beta}{U^2} \left[c c_{0\alpha} k_\alpha (M_{\alpha 3} + M_{\alpha 4}) + c^2 c_{0q} k_q M_q \right]$$

$$\dot{M}_{C1} + \lambda_5 M_{C1} = \lambda_5 c_{\infty q} c w' \qquad \dot{M}_q + \lambda_q M_q = \lambda_q \dot{w}'$$

$$\dot{M}_{\alpha 3} + \lambda_{\alpha 3} M_{\alpha 3} = \lambda_{\alpha 3} b_3 A_3 \dot{w} \qquad \dot{M}_{\alpha 4} + \lambda_{\alpha 4} M_{\alpha 4} = \lambda_{\alpha 4} b_4 A_4 \dot{w}$$

$$\lambda_5 = (2U/c) b_5 \beta^2 \qquad \lambda_q = U/(cMk_q)$$

$$\lambda_{\alpha 3} = U/(cMk_\alpha b_3) \qquad \lambda_{\alpha 4} = U/(cMk_\alpha b_4)$$

$$c_{d_{US}} = \frac{1-\eta}{c_{\ell\alpha}} \left[(c_\ell + c_{\ell_{US}}) \left(c_\ell + \frac{a}{U} (L_{C1} + L_{C2}) \right) - c_\ell^2 \right] - \frac{1}{c_{\ell\alpha}} \left[(c_\ell + c_{\ell_{US}}) \frac{a}{U} (L_{C1} + L_{C2}) \right]$$

where $A_1 = .3$, $A_2 = .7$, $A_3 = 1.5$, $A_4 = -.5$, $b_1 = .14$, $b_2 = .53$, $b_3 = .25$, $b_4 = .1$, $b_5 = .5$. The time constants are:

$$T = 2Mk = 2M \frac{c_0 \kappa}{c_1(1-M) + c_\infty 2M^2 \beta \sum(Ab)}$$

where $\sum(Ab)$ is $A_1 b_1 + A_2 b_2 = .413$ for the lift; b_5 for the moment k_q ; and zero for the moment k_α . The factors κ are introduced to improve correlation with measured loads. Good results are obtained with $\kappa_L = .75$ for lift and $\kappa_M = .80$ for moment. The constants c_0 , c_1 , and c_∞ are given in the following table.

derivative	load	$2\pi c_0$	$2\pi c_1$	$2\pi c_\infty$
α	c_ℓ	4	4	2π or $c_{\ell\alpha}$
	c_m	-1	-1	0 or $c_{m\alpha}$
$q = \dot{\alpha}c/U$	c_ℓ	1	1	π
	c_m	$-\frac{7}{12}$	$-\frac{5}{4}$	$-\frac{\pi}{8}$

The expressions for c_1 are obtained from reference 12. The quasistatic terms of incompressible thin-airfoil theory give c_∞ . Optionally the α derivatives for c_∞ can be evaluated from the airfoil tables (then $a = 2\pi/\beta$ should be used). In $c_{d_{US}}$, c_ℓ is the lift coefficient without the unsteady load or dynamic stall terms. The unsteady drag is based on approximating the steady drag in attached flow as follows (ref. 21): $c_d = c_{dz} + ((1-\eta)/c_{\ell\alpha}) c_\ell^2$, where $\eta < 1$ is the chord force recovery factor (typically

$\eta = .95$) and c_{dz} is the drag at zero lift. The following options are implemented for the drag recovery factor η : (1) constant; (2) from the airfoil table at small angle of attack; (3) from the airfoil table at the local angle of attack. The Leishman-Beddoes theory as presented in ref. 11 uses the secant slope for a in the L_C terms, and the Prandtl-Glauert option in the remaining terms; and the aerodynamic center and drag recovery factor from the airfoil tables at the local angle of attack.

APPENDIX B: Dynamic Stall

This appendix presents the equations for the dynamic stall models of CAMRAD II. Dynamic stall models from Johnson, Boeing, Leishman-Beddoes, ONERA EDLIN, and ONERA BH are included. Dynamic stall is characterized by a delay in the occurrence of separated flow produced by the wing motion, and high transient loads induced by a vortex shed from the leading edge when stall does occur. Let α_d be the delayed angle of attack, calculated from the angle of attack α . Then the corrected coefficients are:

$$\begin{aligned} c_\ell &= \left(\frac{\alpha - \alpha_z}{\alpha_d - \alpha_z} \right) c_{\ell_{2D}}(\alpha_d) + \Delta c_{\ell_{DS}} \\ c_d &= \left(\frac{\alpha - \alpha_z}{\alpha_d - \alpha_z} \right)^2 \left(c_{d_{2D}}(\alpha_d) - c_{dz} \right) + c_{dz} + \Delta c_{d_{DS}} \\ c_m &= \left(\frac{\alpha - \alpha_z}{\alpha_d - \alpha_z} \right) \left(c_{m_{2D}}(\alpha_d) - c_{mz} \right) + c_{mz} + \Delta c_{m_{DS}} \end{aligned}$$

where α_z is the zero-lift angle of attack, and c_{dz} and c_{mz} are the corresponding drag and moment. The form of the lift and moment corrections ensures that the coefficients below stall are unchanged. The Δc_{DS} 's are increments defined by the dynamic stall model, generally attributed to the leading-edge vortex. The dynamic stall effects are washed out for angles of attack near ± 90 . When implemented, the appropriate changes for negative angle of attack and reverse flow are included in all models.

Johnson Model

The Johnson dynamic stall model (adapted from ref. 14) uses an angle of attack delay proportional to $\dot{\alpha}$, plus impulsive lift and moment increments from the leading-edge vortex. The angle of attack is evaluated with a time delay $\Delta t = \tau_d c / 2U$ that accounts for the hysteresis effects around stall: $\alpha_d = \alpha(t - \Delta t) \cong \alpha - \Delta t \dot{\alpha} = \alpha - \tau_d \dot{\alpha} c / 2U$. Alternatively, α_d is the solution of a state equation: $\dot{\alpha}_d + \lambda_d(\alpha_d - \alpha_z) = \lambda_d(\alpha - \alpha_z)$, where $\lambda_d = 2U / c\tau_d$. McCroskey (ref. 15) and Beddoes (ref. 16) found that the dynamic stall delay correlates fairly well in terms of the normalized time constant τ_d . The values $\tau_L = 9.2$ and $\tau_M = 5.4$ are typical. The equations for the loads include the increments $\Delta c_{\ell_{DS}}$, $\Delta c_{d_{DS}}$, and $\Delta c_{m_{DS}}$, which are produced by the leading-edge vortex. When the blade section angle of attack reaches the dynamic stall angle α_{DS} , a leading-edge vortex is shed. As this vortex passes aft over the airfoil upper surface it induces large transient loads. The experimental data of reference 17 show that the peak incremental aerodynamic coefficients depend on the pitch rate at the instant of stall, $\dot{\alpha}c/U$. It is assumed that the incremental coefficients caused by the shed vortex (Δc_{DS}) rise linearly to these peak values in the time increment $\Delta t_{DS} = \tau_v c / 2U$, and then fall linearly to zero in the time Δt_{DS} again. Hence the model involves impulsive lift and nose down moment changes when dynamic stall occurs. After these transient loads decay, the wing section is assumed to be in deep stall, and dynamic stall is not allowed to occur again until the flow has reattached. Flow reattachment takes place when the angle of attack drops below the angle α_{RE} . The dynamic stall angle α_{DS} and reattachment angle α_{RE} correspond to $f_d = f(\alpha_d) = .7$, where f is the trailing-edge separation point of the Leishman-Beddoes model. The experimental data of reference 17 give $\Delta c_{\ell_{LEV}} = 2.0$ and $\Delta c_{m_{LEV}} = -0.65$ for the peak loads at high pitch rate ($\dot{\alpha}c/U$ at stall above .05). Typically $\tau_v = 3.6$ to 5.6. Note that if the total rise and fall time $2\Delta t_{DS}$ is interpreted as the time the leading-edge vortex takes to traverse the chord (distance c), then the speed of the vortex is $v_{\text{vortex}} = U / \tau_v$. So $\tau_v = 4$ implies the leading-edge vortex travels at one-fourth the free stream speed.

Boeing Model

The Boeing dynamic stall model (developed in refs. 18 to 20) uses an angle of attack delay proportional to the square-root of $\dot{\alpha}$, which produces the basic hysteresis effects. The coefficient increments produced by the leading-edge vortex are not used in this model. The delayed angle of attack is $\alpha_d = \alpha - \tau_d \sqrt{|\dot{\alpha}c/2U|} \text{sign } \dot{\alpha}$. Alternatively, this can be considered a time lag dependent on the pitch rate, giving a state equation for α_d : $\dot{\alpha}_d + \lambda_d(\alpha_d - \alpha_z) = \lambda_d(\alpha - \alpha_z)$, where $\lambda_d = (2U/c\tau_d) \sqrt{|\dot{\alpha}c/2U|}$. The time constant τ_d is a function of Mach number and the airfoil section, obtained from oscillating airfoil tests (ref. 20).

Leishman-Beddoes Model

The Leishman-Beddoes dynamic stall model (refs. 21 to 23) uses a delayed angle of attack, plus lift and moment increments from the leading-edge vortex. This model characterizes the airfoil static stall behavior by the trailing-edge separation point f (fraction of chord from leading edge), and a critical lift coefficient $c_{\ell_{CR}}$ at the separation onset boundary (leading-edge separation at low Mach number, shock reversal at high Mach number). The airfoil data for lift are used to identify constants s_1 , s_2 , and α_s that generate $f(\alpha)$ as follows:

$$f = \begin{cases} 1 - .3 \exp((|\alpha - \alpha_z| - \alpha_s)/s_1) & |\alpha - \alpha_z| \leq \alpha_s \\ .04 + .66 \exp((\alpha_s - |\alpha - \alpha_z|)/s_2) & |\alpha - \alpha_z| > \alpha_s \end{cases}$$

Then $|\alpha - \alpha_z| = \alpha_s$ or $f = .7$ is taken as the definition of stall. The parameters $c_{\ell_{CR}}$, s_1 , s_2 , and α_s are required as a function of Mach number, for positive and negative angle of attack, normal and reverse flow, at each span station. The Leishman-Beddoes model for unsteady flow is based on $f_d = f(\alpha_d)$ at the delayed angle of attack. Here the model is modified to use the static loads directly from the airfoil tables, instead of fitting the static loads to analytical functions. Further modifications of the model are required because the above expression for $f(\alpha)$ does not distinguish between positive and negative angle of attack. The model is also extended to large angle of attack and reverse flow. In order to handle oscillations through α_z , a continuous monotonic function of α is needed:

$$\hat{f} = \begin{cases} f_z - f & \alpha - \alpha_z \geq 0 \\ f - f_z & \alpha - \alpha_z < 0 \end{cases}$$

where $f_z = f(\alpha_z) = 1 - .3 \exp(-\alpha_s/s_1)$; note that f_z may not be the same for positive and negative angle of attack. In order to handle large angle of attack, the function f is modified:

$$f = \begin{cases} 1 - .3 \exp((|\alpha - \alpha_z| - \alpha_s)/s_1) & |\alpha - \alpha_z| \leq \alpha_s \\ .04 + .66 \exp((\alpha_s - |\alpha - \alpha_z|)/s_2) & |\alpha - \alpha_z| > \alpha_s \\ f_H(90 - |\alpha - \alpha_z|)/(90 - \alpha_H) & |\alpha - \alpha_z| > \alpha_H \end{cases}$$

Here $\alpha_H = \alpha_s + Hs_2$ and $f_H = .04 + .66e^{-H}$, and $H = 6$ is used. This modification to the definition of f does not affect the model for attached flow or around stall, but with it the delayed angle of attack behaves reasonably at very large angles.

The delayed angle of attack α_d is calculated as follows. Static hysteresis around stall is modelled by using a smaller α_s when the angle of attack is decreasing: $\alpha_s = \alpha_{s \text{ input}} - \Delta\alpha_s(1 - f_d)^{1/4}$ (with f_d from the last time step). There is a lag in the leading-edge pressure relative c_ℓ , so a lagged lift is used in the stall criterion:

$$\begin{aligned} \dot{L}_p + \lambda_p L_p &= \lambda_p(\alpha - \alpha_z + L_C/A) \\ \alpha_p &= L_p + L_I/A + \alpha_z \end{aligned}$$

where $A = c_{\ell_\alpha}$. The dimensionless time constant T_p gives $\lambda_p = 2U/cT_p$. The unsteady lift $c_{\ell_{US}}$ is split into L_C (the $L_{C1} + L_{C2}$ term in Leishman-Beddoes theory) and L_I (the remaining terms), calculated using $a = c_{\ell_\alpha}$ instead of the secant slope. The stall

criterion is based on $c_{\ell p} = A(\alpha_p - \alpha_z)$. If $|c_{\ell p}| \geq c_{\ell CR}$, the critical condition for leading-edge or shock-induced separation has been reached; while if $|c_{\ell p}| < c_{\ell CR}$, reattachment is allowed. This angle of attack gives a trailing-edge separation point $\hat{f}_p = \hat{f}(\alpha_p)$. There is an additional lag in the boundary layer response, modelled as a lag in f :

$$\dot{\hat{f}}_d + \lambda_f \hat{f}_d = \lambda_f \hat{f}_p$$

where $\lambda_f = 2U\sigma_f/cT_f$. There are separate f_d equations for lift and moment, to allow different behavior during reattachment (implemented using different values of σ_f). If f_d is decreasing ($\Delta f_d < 0$), the flow is separating; if f_d is increasing, the flow is reattaching. The difference Δf_d is calculated at the end of the procedure, for use during the next time step. Finally, the delayed angle of attack α_d is calculated from \hat{f}_d . Vortex lift accumulation begins at the onset of stall (indicated by $|c_{\ell p}| = c_{\ell CR}$), driven by the difference between the linear and nonlinear lifts: $c_v = c_{\ell L} - c_{\ell} = A(\alpha - \alpha_z) - c_{\ell}$. The leading-edge vortex reaches the trailing edge at time $\tau_{DS} = T_{vl}$, where $t_{DS} = \tau_{DS}c/2U$ is the time since the onset of stall. The speed of the vortex implied is $v_{\text{vortex}} = 2U/T_{vl}$, or one-fourth the free stream velocity for $T_{vl} = 8$. The vortex loads are obtained from c_v with a time lag:

$$\begin{aligned} \dot{L}_v + \lambda_v L_v &= D\dot{c}_v & \Delta c_{d_{DS}} &= L_v \tan(\alpha - \alpha_z) \\ \Delta c_{\ell_{DS}} &= L_v & \Delta c_{m_{DS}} &= -x_s \left(1 - \cos \frac{\pi \tau_{DS}}{T_{vl}}\right) \Delta c_{\ell_{DS}} \end{aligned}$$

where $x_s = .20$ or $.25$ typically. The moment exists only until $\tau_{DS} = 2T_{vl}$. The time constant gives $\lambda_v = 2U\sigma_v/cT_v$. The switch D (equal zero or one) turns the vortex lift accumulation on and off. With the switch D present, it is not possible to formulate the equation for L_v in terms of c_v instead of \dot{c}_v , such that the CAMRAD II analysis can deal with the resulting differential equation of motion. So an implicit solution is always used for L_v . Interactions between the mechanisms are accounted for by modifying the time constants, using the parameters σ_f (for lift and moment) and σ_v .

An alternative form of the delayed angle of attack calculation uses a lagged lift coefficient $c_{\ell p}$ to obtain the angle of attack α_p :

$$\begin{aligned} c_{\ell C} &= A(\alpha - \alpha_z) + L_C & c_{\ell p} &= L_p + L_I \\ \dot{L}_p + \lambda_p L_p &= \lambda_p c_{\ell C} & \alpha_p &= c_{\ell p}/A + \alpha_z \end{aligned}$$

To match the implicit solution of the Leishman-Beddoes model in references 21 and 22, the following form is required:

$$\begin{aligned} c_{\ell C} &= A(\alpha - \alpha_z) + L_C & c_{\ell p} &= c_{\ell C} - L_p + L_I & \dot{L}_f + \lambda_f L_f &= \dot{\hat{f}}_p \\ \dot{L}_p + \lambda_p L_p &= \dot{c}_{\ell C} & \alpha_p &= c_{\ell p}/A + \alpha_z & \hat{f}_d &= \hat{f}_p - L_f \end{aligned}$$

The time derivatives on the right hand side of these state equations are not available analytically, so in this form an implicit solution must be used. In practice, identical results are obtained from all these forms of the equations.

The trailing-edge separation point f is related to the airfoil lift using the Kirchhoff expression: $c_{\ell} = c_{\ell\alpha} ((1 + \sqrt{f})/2)^2 (\alpha - \alpha_z)$ (ref. 21). Hence the airfoil table data for lift define f as a function of α . The parameter α_s is given by $f = .7$; and then s_1 and s_2 are identified by fitting the table data. The critical lift $c_{\ell CR}$ should be identified from pressure data (ref. 21), but can also be determined based on the break in chord force (loss of leading-edge suction) or the sudden increase in drag. The time constants are determined by correlation with unsteady airfoil data (see, for example, ref. 22).

ONERA EDLIN Model

The ONERA EDLIN (Equations Differentielles Lineaires) dynamic stall model (ref. 6) uses a stall delay, plus lift, drag, and moment increments calculated from second-order differential equations:

$$\begin{aligned} \ddot{L}_2 + a\dot{L}_2 + bL_2 &= -bU \Delta c_{\ell} - eU \dot{\alpha} \\ \ddot{M}_2 + a\dot{M}_2 + bM_2 &= -bU \Delta c_m - eU \dot{\alpha} \\ \ddot{D}_2 + a\dot{D}_2 + bD_2 &= -bU \Delta c_d - eU \dot{\alpha} \text{sign}(\alpha - \alpha_z) \end{aligned}$$

with α in degrees here. These equations are driven by the difference between the linear and nonlinear loads: $\Delta c_\ell = c_{\ell L} - c_\ell = c_{\ell\alpha}(\alpha - \alpha_z) - c_\ell$, $\Delta c_m = c_{mL} - c_m = c_{m\alpha}(\alpha - \alpha_z) + c_{mz} - c_m$, $\Delta c_d = c_{dL} - c_d = c_{dz} - c_d$; where c_ℓ , c_m , and c_d are here the static coefficients, without the unsteady or leading-edge vortex terms. Then the load increments are

$$\begin{aligned}\Delta c_{\ell_{DS}} &= \frac{1}{U} (L_2 + U \Delta c_\ell + dU \dot{\alpha}) \\ \Delta c_{m_{DS}} &= \frac{1}{U} (M_2 + U \Delta c_m + dU \dot{\alpha}) + M_3 \\ \Delta c_{d_{DS}} &= \frac{1}{U} (D_2 + U \Delta c_d + dU \dot{\alpha} \text{sign}(\alpha - \alpha_z))\end{aligned}$$

The stall delay is accounted for by setting the right-hand side of the differential equation to zero if $\tau_{SS} < \tau_d$, where $t_{SS} = \tau_{SS}c/2U$ is the time since the static stall angle was exceeded. The static stall angle corresponds to $f(\alpha) = .7$, where f is the trailing-edge separation point of the Leishman-Beddoes model. Petot has described a refined transition model, intended to accommodate airfoils that exhibit larger nose-down pitching moments at dynamic stall. The refined transition model assumes that the extra lift from dynamic stall is convected aft from the quarter chord after moment stall occurs, producing the extra moment term M_3 in $\Delta c_{m_{DS}}$. Here this refined transition model is implemented by

$$M_3 = -(\tau_{SS} - \tau_{dM}) \mu \Delta c_{\ell_{DS}}$$

for $(\tau_{SS} - \tau_{dM})\mu = 0$ to 1.5 (convection from quarter chord to trailing edge). This extra moment is turned off after lift stall, by multiplying M_3 by the factor $(2 - \tau_{SS}/\tau_{dL})$ when $\tau_{dL} < \tau_{SS} < 2\tau_{dL}$. The coefficients in these equations depend on the lift difference Δc_ℓ :

$$\begin{aligned}a &= (2U/c) (a_0 + a_2(\Delta c_\ell)^2) \\ b &= (2U/c)^2 (b_0 + b_2(\Delta c_\ell)^2)^2 \\ e &= (2U/c) e_2(\Delta c_\ell)^2\end{aligned} \quad d = \begin{cases} (c/2U) d_1 |\Delta c_\ell| & \text{lift and moment} \\ (c/2U) (d_0 |\alpha - \alpha_z| + d_1 |\Delta c_\ell|) & \text{drag} \end{cases}$$

The notation has been changed somewhat from the original ONERA notation. The parameters must be evaluated from data on airfoils oscillating in the stalled flow regime (see, for example, ref. 6).

ONERA BH Model

The ONERA BH (Bifurcation de Hopf) dynamic stall model (ref. 24) uses a delayed angle of attack, plus lift and moment increments calculated from first-order and second-order differential equations:

$$\begin{aligned}\dot{L}_1 + \lambda L_1 &= -\lambda U \Delta c_\ell & \ddot{L}_2 + a \dot{L}_2 + b L_2 &= eU \dot{\alpha} + dU \ddot{\alpha} \\ \dot{M}_1 + \lambda M_1 &= -\lambda U \Delta c_m & \ddot{M}_2 + a \dot{M}_2 + b M_2 &= eU \dot{\alpha} + dU \ddot{\alpha}\end{aligned}$$

with α in degrees here. Then the load increments are

$$\begin{aligned}\Delta c_{\ell_{DS}} &= \frac{1}{U} (L_1 + U \Delta c_\ell + L_2) \\ \Delta c_{m_{DS}} &= \frac{1}{U} (M_1 + U \Delta c_m + M_2)\end{aligned}$$

The appropriate changes for reverse flow are included. The delayed angle of attack is calculated using a simplified version of the Leishman-Beddoes model:

$$\begin{aligned}\dot{\alpha}_p + \lambda_p(\alpha_p - \alpha_z) &= \lambda_p(\alpha - \alpha_z) & \dot{\hat{f}}_d + \lambda_f \hat{f}_d &= \lambda_f \hat{f}_p \\ \hat{f}_p &= \hat{f}(\alpha_p) & \alpha_d &= \alpha(\hat{f}_d)\end{aligned}$$

where $\lambda_p = 2U/cT_p$ and $\lambda_f = 2U/cT_f$. The coefficients in these equations depend on the load increments:

$$\begin{aligned} a &= (2U/c) \omega_s (-a_0 + a_2 \Delta c^2) & e &= (2U/c) \omega_s e_0 \\ b &= (2U/c)^2 \omega_s^2 (1 - b_1 \Delta c \text{sign}(\alpha - \alpha_z) - b_2 \Delta c^2) & d &= \omega_s d_0 \\ & & \lambda &= (2U/c) \lambda_0 \end{aligned}$$

using $\Delta c = L_2/U$ and M_2/U in the lift and moment equations respectively (from the last time step if an implicit solution is used). The notation has been changed somewhat from the original ONERA notation. The parameters have different values for separating and reattaching flow: separating flow values are used if $f_p < f_{CR}$; reattaching flow values are used if $f_p \geq f_{CR}$ (note the use of f_p rather than f_d). For lift, $f_{CR} = .7$ is used. The critical angle of attack is $\Delta\alpha_m$ larger for moment than for lift. So

$$f_{CR} = \begin{cases} .04 + .66 \exp(-\Delta\alpha_m/s_2) & \text{if } \alpha \text{ increasing} \\ 1. - .3 \exp(-\Delta\alpha_m/s_1) & \text{if } \alpha \text{ decreasing} \end{cases}$$

is used for the moment. For reattaching flow, only a_0 has a nonzero value, so the dynamic stall loads decay. The parameters must be evaluated from data on airfoils oscillating in the stalled flow regime (see, for example, ref. 24).